Magnetic resonance in quantum spin chains

H.-A. Krug von Nidda[a], N. Büttgen, and A. Loidl

Experimental Physics V, Center for Electronic Correlations and Magnetism, University of Augsburg, 86135 Augsburg, Germany

Abstract. The present understanding of quantum spin chains is reviewed from the magnetic resonance point of view. This includes both the ideal one-dimensional properties in the spin sector as well as the complex interplay with orbital, charge, and lattice degrees of freedom which govern the ground state. In copper-phosphates we observe an extremely extended paramagnetic regime governed by strong antiferromagnetic correlations with record values of the ratio $k_{\mathrm{B}}T_{\mathrm{N}}/J < 6 \times 10^{-4}$, which compares the ordering temperature of a Néel state to the magnitude of the exchange J between neighbouring spins. A detailed quantitative discussion of NMR and ESR relaxation within this paramagnetic regime elucidates the relevant exchange interactions in typical bonding geometries of most common quantum-spin-chain systems like $KCuF_3$, $CuGeO_3$, $Na_xV_2O_5$, and $LiCuVO_4$. Concerning the ground state, paramount topics of modern solid-state physics arise among these examples as there are multiferroicity, charge order, metal-insulator transition, and spin dimerization as well as phase separation.

1 Introduction

In the course of this work, the magnetic properties of one-dimensional (1D) spatial arrangements of localized magnetic moments in transition-metal oxides are studied by means of electron spin resonance (ESR) and nuclear magnetic resonance (NMR) experiments. In many cases the electron spin, which is relevant for the physical properties of the material, can be directly probed by ESR. The intensity of the ESR line represents the pure spin susceptibility. The resonance field yields the Landé-factor g and provides information on internal fields. The linewidth is determined by the spin-spin relaxation due to local anisotropic interactions like dipolar or anisotropic exchange. NMR of appropriate nuclei yields the Knight shift due to the local susceptibility, the electric field gradient (EFG) due to the ligand ions, and nuclear spin-relaxation rates due to the interactions with the electronic system and the lattice. In magnetically ordered phases information on details of the magnetic structure is obtained from characteristic shifts or splitting of NMR and ESR spectra.

For bulk magnets there are universality classes which are determined by the number of spin components n, where the index n is related to the type of magnetic anisotropy. The indices $n = 1$ (Ising), $n = 2$ (XY), and $n = 3$ (Heisenberg) correspond to magnets with easy-axis anisotropy, easy-plane anisotropy, and isotropic magnets without anisotropy, respectively. In order to theoretically describe the magnetic behavior of localized moments, one is restricted either to low-spin values S of the local moments or to low spatial dimensionality: exact solutions of the ground states are given for some specific cases only, such as Bethe's solution [1] to the spatially 1D Heisenberg chain in case of $S = 1/2$ or Onsager's solution [2] to the 2D Ising model on a square lattice.

[a] e-mail: hans-albrecht.krug@physik.uni-augsburg.de

Realizations of low-dimensional spin systems had been discovered earlier in organic salts like tetra-methyl ammonium manganese chloride (TMMC) and the peculiarities of their ESR and NMR properties had been investigated with large experimental and theoretical efforts [3–5]. In recent years the low-dimensional quantum magnetism in transition-metal oxides received much attention. In particular, the discovery of a spin-Peierls transition in the quasi one-dimensional Heisenberg antiferromagnet $CuGeO_3$ in 1993 [6] triggered an intense search for such a ground state in other transition-metal oxides with spin $S = 1/2$ ions like Cu^{2+} or V^{4+}. A spin-Peierls transition is characterized by the opening of an energy gap due to dimerization of every two neighbouring spins forming a non-magnetic singlet state, whereby the unit cell along the chain is doubled. But although such a ground state is often observed in organic chain compounds, no second inorganic spin-Peierls system could be unambiguously identified, except TiOCl which is still under debate [7]. Nevertheless, in this context numerous interesting spin-chain and -ladder oxides were investigated, as there are, e.g., telephone-number compounds $(La : Sr)_{14}Cu_{24}O_{41}$ [8] or the quarter-filled $S = 1/2$ spin-ladder system NaV_2O_5 [9].

The best realizations today of a 1D chain-like arrangement of spins, which can be described within the Heisenberg model of interacting nearest-neighbouring moments, are phosphate compounds like $Sr_2Cu(PO_4)_2$ (Ref. [10]). In order to comprehend the outstanding role of $Sr_2Cu(PO_4)_2$ among 1D systems it is important that nearest-neighbouring Cu^{2+} moments are not linked via Cu-O-Cu super-exchange paths in corner- or edge-sharing geometries.

The aim of this article is to work out characteristics in the paramagnetic regime as well as of the ground states (magnetic order, ferroelectricity, charge order, spin dimerization) of quantum-spin-chain systems ($S \leq 1$) by means of magnetic resonance. We start with the illustration of the local susceptibility in systems with an extended paramagnetic regime governed by strong antiferromagnetic correlations. A detailed quantitative discussion of NMR and ESR relaxation within this paramagnetic regime elucidates the relevant exchange interactions in typical bonding geometries of most common quantum spin chains. Concerning the ground state, we investigate paramount topics of modern solid state physics as magnetic order and ferroelectricity in $LiCuVO_4$, charge order and spin dimerization in NaV_2O_5, and phase separation in the doped spin-Peierls system $(Cu : Mg)GeO_3$.

2 Ideal realization of 1D magnets

It is the strong next-nearest neighbour (NNN) interaction in many edge-shared chain cuprates which prevents these compounds to build an uniform magnetic chain described by a simple nearest-neighbour (NN) Heisenberg model [11,12]. So far the best realizations of quantum spin chains in inorganic materials with dominating NN exchange are among phosphate compounds like $Sr_2Cu(PO_4)_2$ and $Ba_2Cu(PO_4)_2$ (Ref. [10]), where plaquettes of CuO_4 with Cu^{2+} ions ($S = 1/2$) along a crystallographic axis represent chains of magnetic moments which are dominated by NN exchange only. These CuO_4 units are isolated in the sense that the oxygen anions of adjacent plaquettes are not linked by corner- nor edge-sharing entanglement, resulting in vanishingly small NNN interactions.

Figure 1 shows the local and bulk magnetic susceptibilities (i.e. NMR line shift K and volume susceptibility χ, respectively) of a number of copper-phosphates. In the case of $BaCuP_2O_7$, the effect of magnetic impurities (chain ends, natural defects, excess oxygen, and/or extrinsic paramagnetic moments) is seen in the low-temperature region of the bulk susceptibility $\chi(T)$ as a Curie-type contribution with diverging χ values. It is a great advantage of the local susceptibility $K(T)$ obtained in the NMR experiment that it is not affected by these artefacts, but solely coupled to the intrinsic spin susceptibility via the hyperfine coupling A_{hf}. With respect to the crystallographic structure, all these phosphate compounds represent $S = 1/2$ chains of Cu^{2+} cations in CuO_4 units.

The temperature dependences of the NMR line shift $K(T)$ exhibit broad maxima which are indicative of the low-dimensional magnetic behavior. $K(T)$ could nicely be fitted to Johnston's expression [13] of the spin susceptibility $\chi_{1\mathrm{D}}(T)$ for a uniform $S = 1/2$ antiferromagnetic spin chain via $K = A_{\mathrm{hf}} \cdot \chi_{1\mathrm{D}}(T)$ (red solid lines in Fig. 1). These fits revealed that $Sr_2Cu(PO_4)_2$

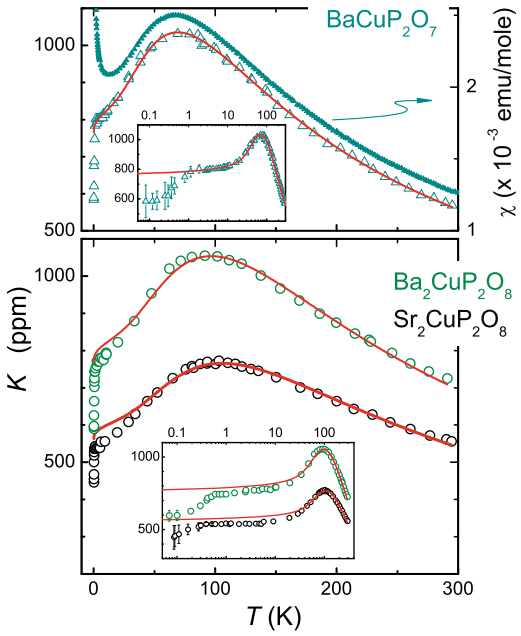

Fig. 1. Line shift K of ^{31}P nuclei and bulk susceptibility χ vs. temperature T in $BaCuP_2O_7$ (upper frame) and $(Ba/Sr)_2Cu(PO_4)_2$ compounds (lower frame), respectively [14]. The NMR irradiation frequency of 95 MHz corresponds to 55 kOe applied magnetic fields. In the insets, the abscissa axes are changed to logarithmic scales. The red solid lines are fits to the spin susceptibility of a uniform $S = 1/2$ AFM Heisenberg chain according to [13]. From these fits, the exchange constants J_1/k_B =108, 151, and 165 K are obtained for $BaCuP_2O_7$, $Ba_2Cu(PO_4)_2$, and $Sr_2Cu(PO_4)_2$, respectively.

exhibits the largest intra-chain exchange interaction $J_1/k_B = 165$ K among the copper-phosphates investigated so far, and no long-range magnetic order has been detected at temperatures above 100 mK (Ref. [14]). These results gave the record value of the ratio $k_B T_N/J_1 < 6\times10^{-4}$, which compares the ordering temperature of a Néel state to the magnitude of the exchange between neighbouring spins and, therefore, serves as a benchmark of the search for 1D magnets with exchange interactions predominantly along one single crystallographic direction. Up to now, Sr_2CuO_3 with $k_B T_N/J_1 = 2.5 \times 10^{-3}$ was considered to be the compound which is closest to the ideal value $k_B T_N/J_1 = 0$ (Ref. [15]). In Sr_2CuO_3, CuO_4 plaquettes are linked by corner sharing oxygen anions along the crystallographic b-axis.

The hopping parameters t_i and t_i^{ic} $(i = 1, 2)$, which denote the neighbouring intra-chain (t) and inter-chain (t^{ic}) paths, respectively, were calculated within a tight-binding model and the corresponding constants J_i of the exchange interactions were derived [10,16]. The indices $i = 1$ and 2 distinguish between NN and NNN paths, respectively. In that theoretical work, the ratio of the strongest intra-chain coupling to the strongest inter-chain coupling for $Sr_2Cu(PO_4)_2$ was found to be $J_1/J_1^{ic} \approx 70$ and the ratio of NN to NNN intra-chain coupling $J_1/J_2 \approx 700$. For $Ba_2Cu(PO_4)_2$, a slightly lower intra-chain coupling was calculated in perfect agreement with the NMR line shift $K(T)$ measurements, as the maximum of $K(T)$ for $Ba_2Cu(PO_4)_2$ appears at a slightly lower temperature. The cuprate Sr_2CuO_3 with corner-shared geometry of CuO_4 units exhibits the ratio $J_1/J_2 \approx 18$ of NN to NNN intra-chain coupling [17] according to an enhanced NNN exchange interaction. Therefore, from the experimental as well as theoretical point of view, the copper-phosphates like $Sr_2Cu(PO_4)_2$ present the best realization of a uniform 1D Heisenberg chain with only NN interaction, and they even are expected to be candidates for the study of effects beyond Bethe's exact analytical solution [10]. Further strengthening of the 1D magnetic behavior has recently been reported for $K_2CuP_2O_7$ [18], where magnetic frustration effects in the inter-chain couplings weaken the inter-chain coupling $(J_1/J_1^{ic} \approx 500)$ in favor of the dominating 1D intra-chain exchange interaction $J_1/J_2 \approx 4900$ (Ref. [18]).

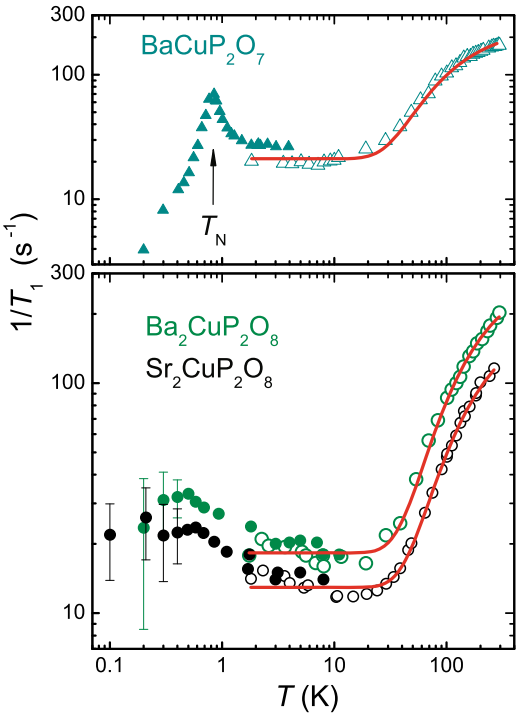

Fig. 2. Spin-lattice relaxation rates $1/T_1$ of ^{31}P nuclei vs. temperature T in $BaCuP_2O_7$ (upper frame), and $(Ba/Sr)_2Cu(PO_4)_2$ compounds (lower frame). The irradiation frequencies of 95 MHz (open symbols) and 6.8 MHz (solid symbols) correspond to 55 kOe (4 kOe) applied magnetic fields, respectively. The red solid lines are fits according to Eq. (1).

The insets of Fig. 1 reveal a steep decrease of the local susceptibility $K(T)$ towards lowest temperatures $T < 0.01\,J_1/k_B$ for all compounds. The spin susceptibility $\chi(T)$ for an uniform $S = 1/2$ antiferromagnetic spin chain (red solid lines in Fig. 1) was found theoretically by Eggert *et al.* to exhibit an asymptotic divergence at low temperatures $\chi_{1D}(T) \propto [\ln(T_0/T)]^{-1}$ with an infinite slope for $T \longrightarrow 0$ with $T_0 \approx 7.7\,J_1/k_B$ [19]. But this infinite slope must not be mistaken for the drop-off of $K(T)$ in the insets of figure 1: as the value of the spin susceptibility $\chi(T = 0)$ at zero temperature is exactly known and a temperature independent value of the chemical shift K_0 is obtained from the fitting with a uniform $S = 1/2$ antiferromagnetic spin chain (red solid lines in Fig. 1), the residual shifts $K = K_0 + A_{hf}\chi(T = 0)$ for $T \longrightarrow 0$ can be calculated. But these theoretical values were found to be *larger* by a factor of 1.3 than the drop-off values of the experimental shifts $K(T \longrightarrow 0)$ (see the insets of figure 1). The origin of this behavior, which seems to be universal in all the phosphate compounds, is not clear up to now. It is most probably not attributed to long-range magnetic ordering or spin dimerization, as there are no additional signatures from other properties supporting the latter scenarios [14,18]. According to Salunke et al. [16], tiny inter-chain interactions yield a change of the spin-spin correlation from power-law behavior to an exponential decay at low temperatures, which is held responsible for the exponential decay of the temperature dependent line shift $K(T)$ towards lowest temperatures $T < 0.01\,J_1/k_B$.

Another explanation of this phenomenon emanates from the assumption that there is a Dzyaloshinskii-Moriya (DM) interaction active between neighbouring copper moments [10]. In the presence of such interactions, the application of an uniform external field H is expected to induce the opening of an energy gap $\Delta \propto H^{2/3}$ in the excitation spectrum of the copper moments. The excitation spectrum then is represented by solitons, antisolitons, and multiple soliton-antisoliton bound states [20]. The excitation modes with the smallest gap values are the so called 'breathers' [20,21] and, probably, such gapped excitation mode accounts for the drastic decrease of $K(T)$ towards lowest temperatures.

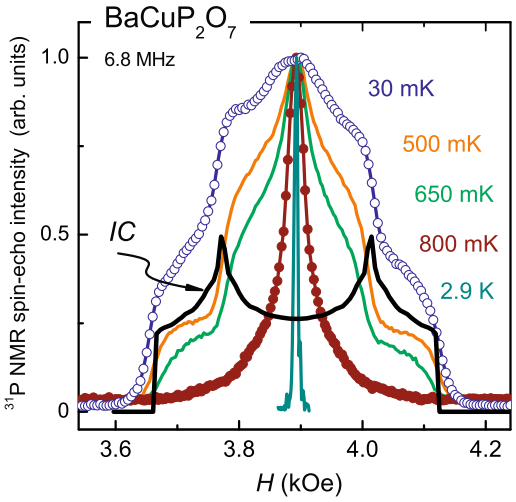

Fig. 3. ^{31}P NMR spectra at 6.8 MHz in $BaCuP_2O_7$. For $T < T_N \approx 850$ mK, the spectra broaden and exhibit a characteristic step-like pattern. The black solid line represents a simulation of an incommensurate magnetic order.

The paramount properties of the copper-phosphates as ideal 1D antiferromagnetic uniform spin chains also allow to test theoretical predictions concerning the dynamics of low-energy spin excitations. For the temperature dependence of the spin-lattice relaxation rate $1/T_1(T)$ (see Fig. 2), Sachdev identified the relevant contributions to $1/T_1$ due to uniform ($q = 0$) and staggered ($q = \pm\pi/a$) spin fluctuations of the dynamic susceptibility $\chi(q,\omega)$ [22]: at low temperatures, the staggered component is expected to dominate $1/T_1$ yielding a temperature independent spin-lattice relaxation rate $1/T_1 = \text{const.}$, whereas the uniform component is expected to govern the spin-lattice relaxation rates at elevated temperatures following a linear relation $1/T_1 \propto T$ [22,23]. Indeed, the experimentally obtained temperature dependences of the spin-lattice relaxation rates $1/T_1(T)$ were in accordance with these theoretical predictions [14,18]. It is important to note that this comparison between theory and experimental results is, strictly speaking, possible up to the upper limit of temperatures $T \approx 0.5 \cdot J_1/k_B$ [23]. At higher temperatures, deviations from the linear relation $1/T_1 \propto T$ are expected.

For higher temperatures, around $T \approx J_1/k_B$ or even above $T > J_1/k_B$, the experimentally obtained spin-lattice relaxation rates $1/T_1$ exhibit saturation as can be seen in figure 2. A parametrization of this temperature dependence of $1/T_1(T)$ is possible with the empirical formula of a thermally activated behavior

$$\frac{1}{T_1}(T) = A \cdot \exp\left(-\frac{J_1}{k_B T}\right) + \frac{1}{T_1^0}. \tag{1}$$

Fits of Eq. (1) to the data are shown by the red solid lines in figure 2, where the prefactors A and the constants $1/T_1^0$ were the only free parameters. The values of the exchange interactions J_1 are fixed to the values [14] that are known from fitting the local susceptibilities $K(T)$ in figure 1. Such an activated behavior, where the energy gaps amount to the same order of magnitude as the exchange interaction J_1, resembles the spin excitation spectrum of solitons in 1D uniform $S = 1/2$ spin chains mentioned above [21]. Further investigations of DM interactions in copper-phosphates as a prerequisite of soliton excitations are highly needed and might explain the low-temperature anomalies in the local susceptibility $K(T)$ and the spin-lattice relaxation rate $1/T_1(T)$ at elevated temperatures, higher than the temperature equivalent of the exchange coupling $T > J_1/k_B$.

In $BaCuP_2O_7$, long-range magnetic order is observed for temperatures $T < T_N \approx 850$ mK [14,24], as the powder spectra broaden and exhibit a characteristic step-like pattern as seen in figure 3. This symmetric multi-step pattern indicates wide distributions of local fields at

the probing nuclear sites, which resembles the characteristics of an incommensurate magnetic ordering. The black solid line represents a simulation of an incommensurate magnetic order according to [25]. As it is elaborated in section 4.1 for the case of $LiCuVO_4$, an incommensurate magnetic order of a one-dimensional spin chain compound is susceptible to a concomitant induction of a ferroelectric moment. Therefore, it is suggestive to speculate about multiferroic behavior in $BaCuP_2O_7$ below 850 mK, for which the underlying mechanism has to be elucidated in future work [it is important to note that the copper cations in $BaCuP_2O_7$ form 1D double uniform chains [26], which clearly differ from the uniform chains in $Sr_2Cu(PO_4)_2$ and $Ba_2Cu(PO_4)_2$].

3 Quasi-1D magnets

So far we have concentrated on NMR results, because the ESR spectra in the above copper-phosphate compounds, which exist in polycrystalline form only, are dominated by the anisotropy of the g-tensor, which is approximately independent on temperature. Thus, the ESR powder pattern is characterized by three peaks at g_x, g_y, and g_z in the regime of 2.0-2.3, whereas the intrinsic linewidth is small compared to the resonance-field distribution corresponding to the g-anisotropy. This results from the fact that the main source of spin-spin relaxation, which determines the linewidth in the 1D copper-phosphates, is due to the dipolar interaction between the copper spins and can be estimated to be of the order of $\Delta H_{\rm dip} \sim 1$ Oe. Therefore, in these compounds ESR basically yields the g-tensor and the intensity (i.e. the spin-susceptibility), but the temperature dependence of the spin-spin relaxation cannot be seriously extracted.

3.1 Universal relaxation

The situation changes remarkably in systems where the super-exchange paths along the chain contain only one diamagnetic ion, like, e.g., in Cu-O-Cu bridges. As two prominent examples we consider $LiCuVO_4$ and $CuGeO_3$: $LiCuVO_4$ crystallizes within an orthorhombically distorted inverse spinel structure, where the magnetic chains are built by equivalent edge-sharing CuO_6 octahedra along the b direction [27,28]. Above 20 K the spin susceptibility is well described by a Bonner-Fisher law [29] with its characteristic maximum near 28 K and a corresponding Heisenberg-exchange constant $J/k_{\rm B} = 45$ K. To lower temperatures the susceptibility is enhanced with respect to the Bonner-Fisher fit and indicates antiferromagnetic order at $T_{\rm N} = 2.1$ K (Refs. [30,31]). In $CuGeO_3$ similar chains of edge-sharing CuO_6 octahedra aligned along the c axis [32,33] determine the quasi-1D magnetic properties ($J/k_{\rm B} = 120$ K). The two oxygen octahedra within the orthorhombic unit cell share the apical oxygen. Hence, there are two inequivalent chains, which differ by the orientation of the octahedron axis in the ab plane and give rise to a sizable inter-chain exchange of about $0.1\,J$. The susceptibility exhibits a maximum near 50 K but fails to follow a Bonner-Fisher law, because of non-negligible NNN interactions [34]. Below the spin-Peierls transition $T_{\rm SP} \approx 14$ K (Ref. [6]) the susceptibility vanishes exponentially due to the singlet formation on dimerization.

Although such compounds are less ideal 1D antiferromagnets, the nuclear- as well as the electron-spin relaxation are still governed by the one-dimensionality. In all cases one observes a single exchange-narrowed ESR line of Lorentz shape near $g = 2$. The right-hand frame of Fig. 4 shows the temperature dependence of the ESR-linewidth in single crystals of the two prototypical spin-chain compounds $LiCuVO_4$ and $CuGeO_3$. For both compounds the linewidth increases monotonously with increasing temperature in the paramagnetic regime and approaches saturation at values larger than 1 kOe in the high-temperature limit. Differences appear only at low temperatures, where the linewidth increases again below the spin-Peierls transition in $CuGeO_3$ and diverges already for $T < 20$ K in $LiCuVO_4$ due to the critical spin fluctuations on approaching magnetic order.

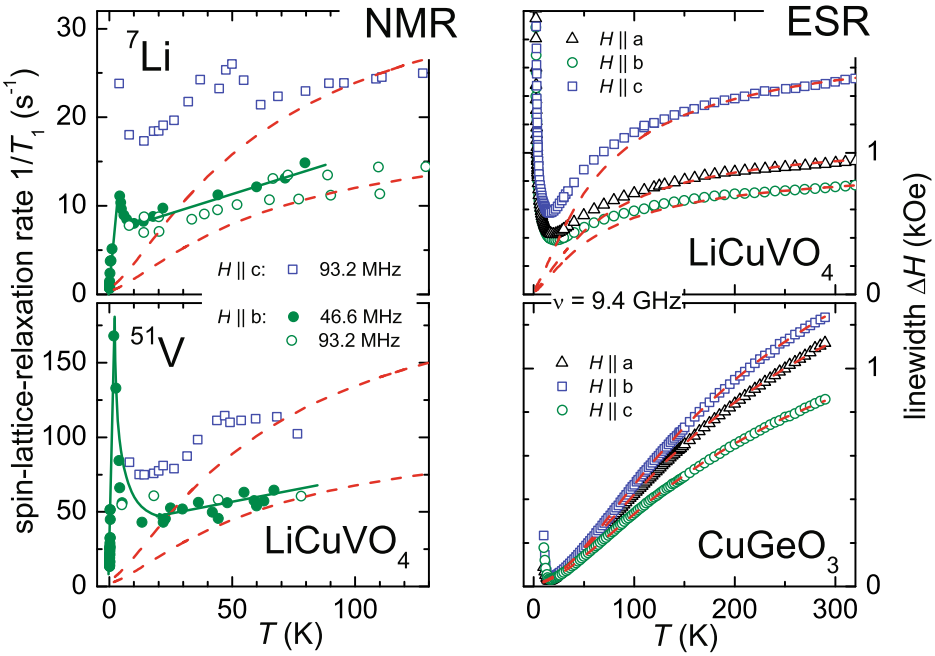

Fig. 4. Temperature dependence of the anisotropic NMR and ESR relaxation rates in single crystals with spin-chains formed by Cu-O_2 ribbons. Left frame: NMR spin-lattice relaxation rates $1/T_1$ for ^{7}Li and ^{51}V in $LiCuVO_4$ (the solid lines are drawn to guide the eye). Right frame: ESR linewidth ΔH for Cu^{2+} in $LiCuVO_4$ and $CuGeO_3$. The dashed lines indicate the empirical law $\Delta H \propto \exp[-C_1/(C_2+T)]$, which is fulfilled in both quantities ($1/T_1$ and ΔH) by the monotonous increase and comparable anisotropy — $LiCuVO_4$: $C_1 = 60(5)$ K, $C_2 = 15(5)$ K, $CuGeO_3$: $C_1 = 235(5)$ K, $C_2 = 40(2)$ K.

In both compounds it is possible to parametrize the temperature dependence of the linewidth above the transition into the ground state by the empirical expression [35]

$$\Delta H(T) = \Delta H_\infty \exp\left(-\frac{C_1}{T + C_2}\right), \tag{2}$$

where ΔH_∞, C_1, and C_2 are treated as fitting parameters. For $LiCuVO_4$ an additional critical divergence $\propto (T - T_N)^{-0.55}$ (not shown in the figure) can account for the broadening on approaching the onset of magnetic order. Note that the parameter C_1 corresponds to the order of magnitude of the isotropic exchange constant. This is reasonable, because the parameter C_1 characterizes the transition from the strongly correlated one-dimensional regime at low temperatures $T \ll J/k_B$ to the purely paramagnetic regime $T \gg J/k_B$ at high temperatures. The parameter C_2 indicates the influence of the low-temperature phase transition on the line broadening. Indeed, Eq. 2 corresponds to the purely activated behavior of Eq. 1 found in the copper-phosphates and suggesting soliton-like excitations, if C_2 approaches zero as expected for ideal 1D antiferromagnets, where magnetic order vanishes.

The left-hand frame of Fig. 4 illustrates the temperature dependence of the NMR spin-lattice relaxation rates of both the ^{7}Li and the ^{51}V nuclei in $LiCuVO_4$. Although the relaxation is strongly governed by the critical fluctuations on approaching magnetic order below 50 K, the monotonous increase and saturation behavior to higher temperatures as well as the anisotropy nicely follow the ESR linewidth. A similar coincidence can be identified for the NMR data in $CuGeO_3$ obtained by Zavidonov and coworkers [36]. Therefore, the NMR spin-lattice relaxation and the ESR linewidth turn out to be driven by the same mechanism.

A similar temperature dependence of the ESR linewidth is observed in two other model compounds with different bonding geometries, namely NaV_2O_5 and $KCuF_3$ as shown in figure 5. In the quarter-filled spin-ladder system NaV_2O_5 the rungs consist of two VO_5 pyramids along

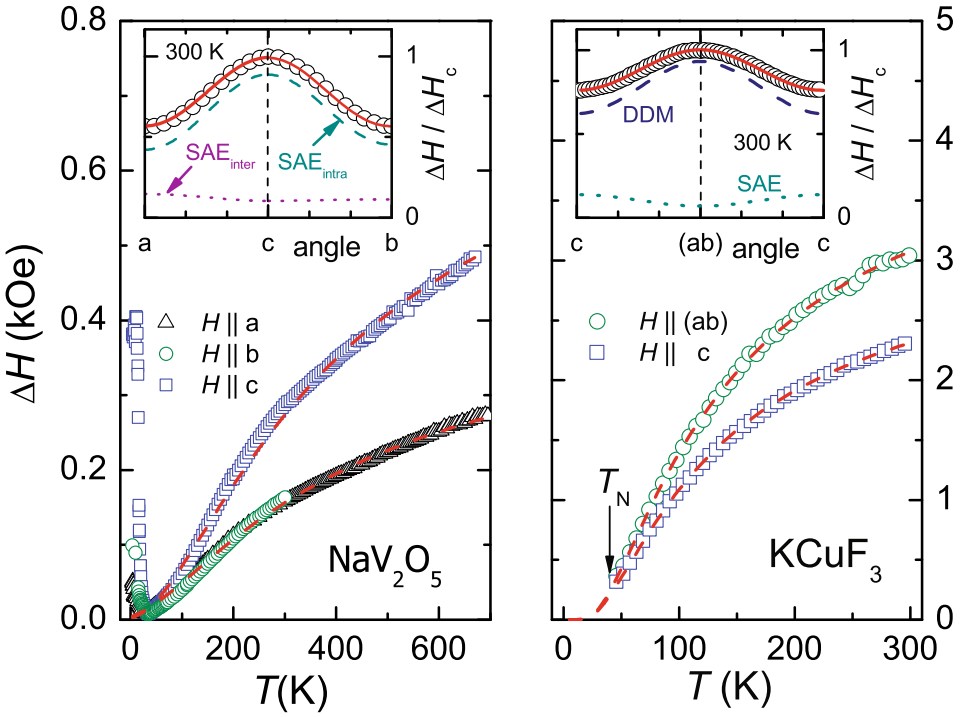

Fig. 5. Temperature dependence of the anisotropic ESR linewidth in single crystals of NaV_2O_5 ($C_1 = 420(20)$ K, $C_2 = 80(10)$ K) and $KCuF_3$ ($C_1 = 116(3)$ K, $C_2 = 0$) – the dashed lines indicate the fit with Eq. 2. Insets: Angular dependence at room temperature $T = 300$ K with contributions of symmetric anisotropic exchange (SAE) (inter- and intra-ladder for NaV_2O_5) and dynamical Dzyaloshinsky-Moriya (DDM) interaction.

the a axis of the orthorhombic structure, which share one corner at their base [37,38]. Each rung carrying one electron is connected with the neighbouring rungs via additional corners at the pyramids' bases forming the ladders along the b axis. The susceptibility is approximately described by a Bonner-Fisher law with $J/k_B = 580$ K but deviates to smaller values at temperatures lower than 200 K (Ref. [39]). Below $T_{CO} \approx 34$ K the susceptibility vanishes exponentially due to the opening of a spin gap of about $\Delta(T = 0)/k_B = 98$ K driven by charge order [40]. In the perovskite system $KCuF_3$ a single hole in the e_g state causes a cooperative Jahn-Teller distortion and occupies alternating $|z^2 - x^2\rangle$ and $|y^2 - z^2\rangle$ orbitals on neighbouring Cu sites along the z direction [41]. The strong overlap of neighbouring orbitals with the intermediate F orbitals results in a large antiferromagnetic exchange $J/k_B = 400$ K giving rise to a Bonner-Fisher law of the magnetic susceptibility. In comparison the overlap of the orbitals within the xy plane, where they also alternate between $|z^2 - x^2\rangle$ and $|y^2 - z^2\rangle$ from site to site, is by far smaller and the corresponding ferromagnetic exchange is weak. Thus, $KCuF_3$ is a good realization of a 1D Heisenberg antiferromagnet, although magnetic order already sets in at $T_N = 40$ K.

In both compounds the linewidth is well parametrized by Eq. (2), however an important difference shows up: while in NaV_2O_5 the parameter C_1 is comparable to the exchange constant J, it turns out to be much smaller than the exchange constant in $KCuF_3$. Moreover, the parameter C_2 vanishes in $KCuF_3$ and the ordering transition does not seem to have any influence on the linewidth. This already indicates that the line broadening in $KCuF_3$ is governed by another relaxation mechanism than NaV_2O_5 and the cuprates mentioned above.

3.2 Anisotropic exchange interactions

An intense, long-lasting debate was carried out concerning the quite large ESR linewidth and the corresponding relaxation processes. An early analysis based on conventional estimates identified

the antisymmetric anisotropic exchange, i.e. the Dzyaloshinsky-Moriya (DM) interaction, as the main source of line broadening in $KCuF_3$ (Ref. [42]), $CuGeO_3$ (Ref. [43]), and NaV_2O_5 (Ref. [44]), exceeding the other possible contributions of symmetric anisotropic exchange and dipole-dipole interaction by factors of 10^2 and 10^3, respectively. However, later on the dominant role of the DM interaction for the line broadening in $S = 1/2$ spin chains came strongly into doubt both for experimental and theoretical reasons: In $LiCuVO_4$ the DM interaction should vanish for symmetry reasons [45], and hence, another source of the line broadening had to be found. Nearly at the same time a theoretical analysis of the high-temperature line broadening in spin $S = 1/2$ chains showed that the DM contribution is only of the same level as the contribution of the symmetric anisotropic exchange [46]. Moreover, a detailed field-theoretical treatment of the low-temperature line broadening in the case of symmetric anisotropic exchange revealed just the monotonous increase of the linewidth on increasing temperature, linear for $k_BT \ll J$, with saturation in the high-temperature limit as experimentally observed in these quasi-1D oxides, while for the antisymmetric DM exchange interaction a divergence $\propto 1/T^2$ is expected at low temperatures [47]. As a consequence, only the symmetric anisotropic exchange interaction was to be considered as the main source of line broadening in these systems. But, how to explain the large high-temperature linewidth, still remained as an open question.

The solution of this problem was triggered by a theoretical analysis of anisotropic super-exchange interactions in chains of edge-sharing CuO_6 octahedra [48], involving two 90° Cu-O-Cu bridges, i.e. a bond geometry where quantum interference between different exchange paths strongly intensifies the anisotropic exchange, which is not taken into account by the conventional estimates. These considerations had been qualitatively suggested to explain the large linewidth observed in the telephone-number compounds $La_{14-x}Ca_xCu_{24}O_{41}$ (Ref. [49]) on the basis of symmetric anisotropic exchange interactions. Such a bond geometry is present also in $CuGeO_3$ and in $LiCuVO_4$. In the latter one, where all Cu sites are equivalent, microscopic quantitative calculations allowed to estimate the magnitude of the symmetric anisotropic exchange and the resulting linewidth has been found to be in very good agreement with the experimental data [50]. Having established the symmetric anisotropic exchange interaction as the main source of line broadening in $LiCuVO_4$, the ESR results in $CuGeO_3$ and NaV_2O_5 could be successfully explained as well.

The theoretical derivation of the anisotropic exchange interactions in spin chains and its application to describe the ESR linewidth in prototypical examples have been recently reviewed in a separate work [51]. Therefore, we shortly summarize only the basic ideas: for the case of strong exchange narrowing [52,53] in the high-temperature limit $k_BT \gg J$ the ESR linewidth

$$\Delta H_\infty = \frac{\hbar}{g\mu_B}\frac{M_2}{\omega_{ex}} \tag{3}$$

is determined by the second moment M_2 of the resonance distribution due to any perturbation like anisotropic exchange or dipolar interactions and the exchange frequency, which can be approximated by $\omega_{ex} \sim J/\hbar$. The angular dependence of the second moment M_2 with respect to the external magnetic field reflects the characteristic anisotropy of the underlying perturbation and, thus, allows to determine the interaction relevant for the spin relaxation.

In $LiCuVO_4$ the leading contribution of the symmetric anisotropic exchange results from the exchange between the $3d_{x^2-y^2}$ excited states of neighbouring Cu ions along the 1D crystallographic b axis connected via two symmetric 90° Cu-O-Cu bonds located within the ab plane: the electron hole (Cu^{2+}, $S = 1/2$) in the $3d_{xy}$ ground state couples to the excited state via spin-orbit coupling λ, is transferred to the excited state of the neighbouring Cu ion through the oxygen $2p$-orbital, returns to the excited state of the starting ion and back to the ground state via spin-orbit coupling. There is only one matrix element $\langle xy \mid l_z \mid x^2 - y^2\rangle = 2i$ of the orbital momentum operator l_z, which connects the $3d_{x^2-y^2}$ and $3d_{xy}$ states. Therefore, this process contributes to the zz diagonal component of the symmetric anisotropic exchange tensor only. The value of the matrix element is estimated as $D_{zz}/k_B \approx -2$ K [50].

The general calculation of the second moment M_2 of symmetric anisotropic exchange can be found in literature [54,55]. If only $D_{zz} \neq 0$, one obtains $M_2(\vartheta) = (\cos^2\vartheta + 1)(D_{zz})^2$, where ϑ denotes the polar angle between the magnetic field H and the z direction which coincides

with the crystallographic c axis in $LiCuVO_4$. Inserted in Eq. 3 with $J/k_B = 45$ K, this yields a linewidth $\Delta H_\infty(\vartheta = 0) \approx 1$ kOe which is twice as large for the magnetic field applied parallel to the crystallographic c axis as compared to the perpendicular orientation. This agrees well with the experimental data at high temperatures shown in figure 4. The residual anisotropy in the ab plane is due to the other smaller matrix elements of anisotropic exchange and dipole-dipole interactions. As a rule, the maximum linewidth appears for the field applied along the direction of the leading matrix element of the diagonalized exchange tensor.

The linewidth in $CuGeO_3$ is dominated by the same symmetric anisotropic exchange within the spin chains. Additional contributions arise from the symmetric anisotropic exchange between the two inequivalent chains [35]. In NaV_2O_5 basically the same $3d$ orbitals like in $LiCuVO_4$ are involved in the leading intra-layer symmetric anisotropic exchange resulting again in the maximum linewidth for the magnetic field applied along the c axis perpendicular to the ladders [56]. The exchange path is slightly different, including exchange both between the excited states and the ground states of neighbouring V ions along the ladder, i.e. the electron couples from the $3d_{xy}$ ground state to the $3d_{x^2-y^2}$ excited state via spin-orbit coupling λ by l_z, is transferred via σ bondings through the oxygen $2p$ orbitals to the excited $3d_{x^2-y^2}$ state of the neighbouring rung, couples via λ to the corresponding $3d_{xy}$ ground state and returns via π-bondings through the oxygen $2p$ orbitals to the $3d_{xy}$ starting orbital. The leading matrix element was estimated as $D_{zz}/k_B \approx 5$ K. For the exact description of the angular dependence, inter-ladder contributions have to be inferred.

In $KCuF_3$ the symmetric anisotropic exchange derived from the orbital configuration yields an inverse anisotropy compared to the observed one. Moreover a static DM interaction can be excluded from the observed temperature dependence. The only possible solution is a dynamic DM interaction resulting from the oscillation of the fluorine ions in the c axis Cu-F-Cu bonds away from 180° (Ref. [57]). The virtual exchange process consists of the excitation of a spin from, e.g., the $3d_{y^2-z^2}$ ground state via spin-orbit coupling into the $3d_{yz}$ excited state of the starting ion, the following hopping into a ground-state orbital on the neighbouring copper ion, and its transfer back into the initial ground-state orbital of the first ion. The corresponding DM vector lies in the ab plane and its absolute value was estimated as $d \approx 5.6$ K. Thus, the maximum linewidth is expected for the magnetic field applied within the ab plane, as observed in the experiment. The pure Arrhenius law observed in the temperature dependence of the linewidth might indicate the thermal excitation of the phonon mode responsible for the dynamical DM interaction. Therefore, the parameter $C_1 = 114$ K derived for $KCuF_3$ is probably not related to the exchange constant J, in contrast to the case of relaxation via the symmetric anisotropic exchange.

Returning to the systems with dominant symmetric anisotropic exchange it is possible to extract important microscopic information on the critical fluctuations on approaching the phase transition into the ground state, i.e. antiferromagnetic order in $LiCuVO_4$, the dimerized spin-Peierls phase in $CuGeO_3$, and the charge-order accompanied by spin-dimerization in NaV_2O_5. As it was discussed in Ref. [47], if the linewidth is determined by only one interaction – in our case the symmetric anisotropic exchange interaction – then the normalized linewidth should be temperature independent. Indeed, as shown in Ref. [51] the linewidth ratios are approximately constant above 40 K, 100 K, and 200 K for $LiCuVO_4$, $CuGeO_3$, and NaV_2O_5, respectively, but below these temperatures distinct systematic changes show up.

In $LiCuVO_4$ this temperature regime coincides with the critical line broadening $\Delta H_{crit} \propto (T - T_N)^{-0.55}$, which becomes sizable already at about $10 \cdot T_N$. Concomitantly on decreasing temperature an enhancement of both longitudinal $1/T_1$ and transversal nuclear magnetic resonance relaxation rates $1/T_2$ is observed on ^{7}Li and ^{51}V nuclei [58]. This is the usual effect, when magnetic order sets in accompanied by critical spin fluctuations. The critical temperature regime is quite broad in comparison with conventional three dimensional systems. The reason may be both due to the one-dimensionality, which favors short-range order, and due to some degree of frustration on the triangular lattice formed in the ac plane by the Cu chains. $CuGeO_3$ and NaV_2O_5 do not exhibit any critical line broadening on approaching the phase transition (only below the transition the ESR line broadens because the exchange narrowing is slowing down with decreasing number of residual non-dimerized spins). Nevertheless, the anisotropy

of the linewidth changes already far above the phase transition. Comparison with other independent experimental methods indicates that the observed deviations result from a change of the exchange integrals due to lattice fluctuations on approaching the spin-Peierls transition in $CuGeO_3$ or charge fluctuations due to the onset of charge order in NaV_2O_5 (Ref. [51]).

3.3 1D metal-to-insulator transition in β-$Na_{1/3}V_2O_5$

An advanced example for application of the knowledge gained on the ESR in prototypical spin-chains presented above is given by the vanadate compound β-$Na_{1/3}V_2O_5$. Its monoclinic crystal structure (space group $C2/m$, lattice parameters $a = 15.40$ Å, $b = 3.61$ Å, $c = 10.05$ Å, $\beta = 109.6°$) contains three inequivalent vanadium sites (V1, V2, V3) which build up three kinds of chains along the crystallographic b direction [59,60]: zigzag chains of edge sharing $V1O_6$ octahedra, two-leg ladders of corner sharing $V2O_6$ octahedra, and zigzag chains of edge sharing $V3O_5$ square pyramids. The Na atoms, which are located in tunnels along the b axis as well, each provide one electron per six vanadium sites yielding a nominal ratio 1:5 of V^{4+} (electron configuration $3d^1$, spin $S = 1/2$) and V^{5+} ($3d^0$, $S = 0$), respectively. Despite the system is crystallographically characterized already since fifty years, the metal-insulator transition at $T_{MI} = 132$ K (Ref. [61]) and pressure induced superconductivity at $T_{sc}(p = 80\,\text{kbar}) = 8$ K (Ref. [62]) have been discovered only a few years ago. As the conductivity is strongly anisotropic with metallic characteristics above T_{MI} along the b direction, only recently grown high-quality single crystals with exact Na stoichiometry allowed for precise resistivity measurements [63].

The nature of the metal-insulator transition and corresponding charge distribution is heavily under debate: above T_{MI}, NMR [64,65] and photoemission spectroscopy [66] identify V1 and V2 sites as possibly mixed valent. Below T_{MI}, different charge-order scenarios are suggested: NMR leaves the question open, whether the electrons condensate on V1 or V2 sites [64]. A linear chain occupation of V1 sites is favoured by theoretical considerations [67], but low-temperature x-ray investigations [68] indicate a block-wise occupation of the V2 sites with a $6b$ periodicity along the b direction. Early ESR measurements [69–73] indicate the electrons to occupy preferentially the V1 sites, but do not reveal the signature of the metal-insulator transition, probably because of the deviations in Na stoichiometry.

Thus, the reinvestigation of the ESR in stoichiometric single crystals of β-$Na_{1/3}V_2O_5$ yielded new important information on the electronic occupation and charge-order pattern. The temperature dependence of the resonance linewidth shown in the left column of Fig. 6 reminds of that observed in α'-NaV_2O_5 but exhibits a strong anomaly on approaching T_{MI} from below. Above the critical regime due to the onset of long-range antiferromagnetic order at $T_N = 24$ K, the linewidth increases monotonously with slightly negative curvature as typically observed in systems, where the relaxation is dominated by symmetric anisotropic exchange. (For $T < T_N$ the magnetic structure has been characterized by detailed antiferromagnetic resonance (AFMR) studies [74].) At about 100 K the curvature changes its sign into positive and the linewidth rapidly increases up to the transition into the 1D-metallic regime at T_{MI}. Above T_{MI} the negative curvature returns and the linewidth saturates like in the prototypical spin chains. To extract the anomaly at the metal-insulator transition, the temperature dependence of the linewidth below the inflection point near 100 K is approximated by the phenomenological expression Eq. (2) and extrapolated to the whole temperature regime. Subtraction of the fit result from the data yields an Arrhenius law compatible with the electrical conductivity. This clearly indicates the switching between the the low-temperature charge-ordered state and the high-temperature conducting state by thermal activation of the charge carriers. The details of electronic configurations are derived from the simultaneous analysis of the anisotropy of g-tensor and linewidth below and above T_{MI} as depicted in the right column of fig. 6.

The g-tensor is smaller than the free electron value for all orientations as typical for a less than half-filled $3d$ shell with quenched orbital momentum. The minimum value, i.e. strongest g shift, is found within the monoclinic ac-plane at about 50° rotated from the a axis in direction to the c axis which is located at 109.6°. This direction approximately coincides with the V1-O4 bond which exhibits the smallest bond length within the $V1O_6$ octahedron. As the strongest g shift is usually expected to appear for the magnetic field applied along the local axis of axial

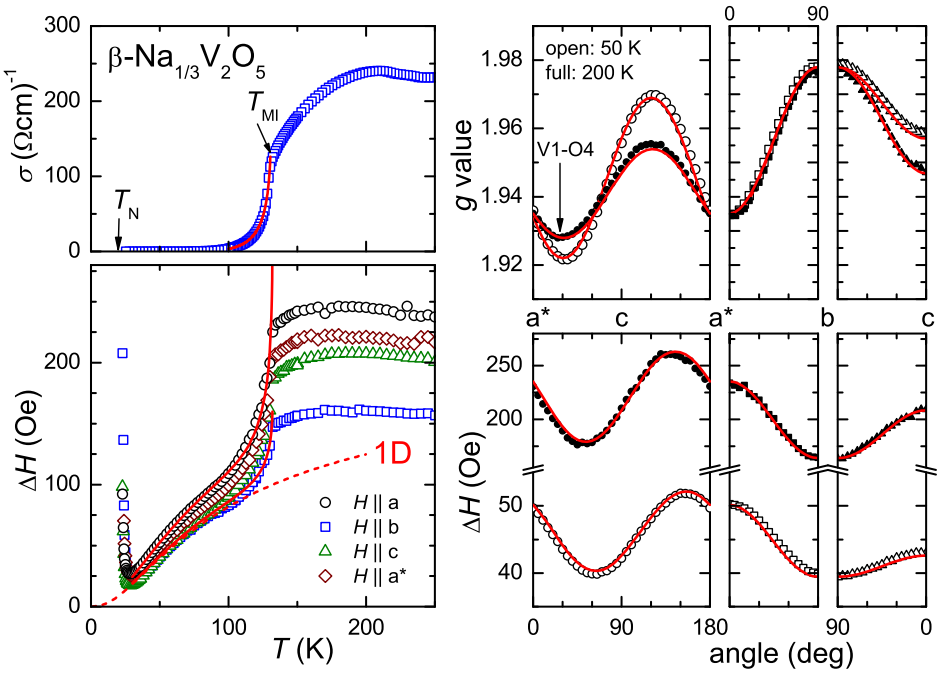

Fig. 6. Left column: temperature dependence of the electrical conductivity σ along the one-dimensional b axis (upper frame) and ESR-linewidth ΔH (lower frame) in $Na_{1/3}V_2O_5$. Right column: angular dependences of g value and linewidth. The fit curves are described in the text. The solid line in σ indicates an Arrhenius law with temperature dependent energy gap, as described in the text. The dashed line in ΔH represents the dependence expected for a linear chain with relaxation governed by symmetric anisotropic exchange using Eq. (2), which together with the Arrhenius law of the conductivity yields the solid lines in ΔH.

distortion, the observed g-tensor indicates that the electrons occupy primarily the $V1O_6$ octahedra. The shortest bond length of the $V2O_6$ octahedron is also located within the ac-plane but perpendicular to the V1-O4 bond, i.e. in the case of preferential occupation of the V2 places the strongest g shift should appear just perpendicular to the observed case. Comparing the g-tensors below and above the metal-insulator transition it turns out that the absolute anisotropy does not change whereas the anisotropy within the ac plane decreases due to an increasing g shift along the direction perpendicular to the V1-O4, i.e. parallel to the V2-O6 bond. This is a hint that in the metallic state the V2 sites become partially occupied. Looking at the crystal structure this is quite reasonable, because the V1-V2 distance of 3.13 Å is indeed smaller than the V1-V1 distance of 3.32 Å and $V2O_6$ ladders are edge sharing with the $V1O_6$ chains.

The picture is completed by considering the anisotropy of the resonance linewidth. For the case that the electrons occupy the V1 place, theoretical predictions expect a linear chain configuration for the charge-ordered state, i.e. every second site of the zigzag chain is occupied by one electron. However, with the symmetric anisotropic exchange as the dominant source of line broadening, it is not possible to describe the linewidth data within such a linear V1 bond geometry. The principal axes of the anisotropic exchange tensor have just to follow the bond geometry which severely restricts the possibilities of the fit. Only for a zigzag bond geometry the data can be satisfactorily described in terms of symmetric anisotropic exchange. At high temperatures a statistical occupation of the V1 sites is assumed, which at low temperature transforms into a six-pack charge-order pattern, i.e. six V1 sites occupied followed by six unoccupied sites in agreement with the $6b$ modulation of the crystal structure found below T_{MI} by x-ray investigations. Note that this six-pack formation describes just the extreme case of a charge-density wave with $6b$ modulation, which is also in agreement with the ESR data.

Finally, one should focus again on the Arrhenius law extracted from the temperature dependence of the linewidth after subtraction of the empirical spin-chain behaviour: a refined analysis of both conductivity and linewidth below T_{MI} in terms of a BCS-like mean-field approach with temperature dependent energy gap $\Delta = 1.74\Delta_0(1 - T/T_{\mathrm{MI}})^{1/2}$ yields a gap-value Δ_0/k_{B} of 475 K and 424 K, respectively. Thus, the ratio $2\Delta_0/k_{\mathrm{B}}T_{\mathrm{MI}} = 6.4 - 7.1$ is strongly enhanced with respect to the BCS value of 3.52. This supports the picture of a charge-density wave formation, but without concomitant spin gap, because the susceptibility shows only a weak anomaly but no exponential drop-off below the metal-insulator transition. This fact indicates a strong on-site Coulomb interaction which may lead to spin-charge separation in a partially occupied chain.

This example shows, how many important microscopic information can be extracted from electron-spin resonance in 1D antiferromagnets. Further interesting applications to be mentioned here, are the dynamic Jahn-Teller effect in $CuSb_2O_6$ (Ref. [75]), the spin dynamics in TiOCl (Ref. [76]), and the dimer formation in $CuTe_2O_5$ (Ref. [77]), which are discussed in the respective references.

4 Characterization of the ground state

4.1 Multiferroicity

Concerning the ground state it is proven by Mermin and Wagner [78] that a spontaneous magnetization accompanied by a long-range magnetic order in a one-dimensional chain-like arrangement of magnetic moments is not possible. Very often, the experimentally observed phenomena of long-range ordered 1D magnets are due to residual, complex interchain couplings of the magnetic moments and the magnetically ordered structure can hardly been calculated theoretically.

Beyond the rare cases where exact solutions are available, the concept of magnetic frustration has found its way into the description of the magnetic ground states in real magnets. In simple terms, magnetic frustration becomes evident when there is a lack of long-range magnetic order despite the fact of strong exchange interactions J between magnetic moments. Magnetic frustration in a 1D chain of spins is induced when there is an antiferromagnetic exchange coupling J_2 between the next-nearest neighbour spins, irrespective of an antiferro- or ferromagnetic coupling J_1 between nearest-neighbour spins. The case of a ferromagnetic coupling J_1 and an antiferromagnetic coupling J_2 is realized in $LiCuVO_4$ where the ground state is a long-range ordered spin helix which propagates along the chain direction. Concomitantly with the formation of the spin helix a spontaneous dielectric polarization occurs. In our NMR experiments we flipped the plane of the spin helix with the externally applied magnetic field and our results are in agreement with theoretical concepts involving the inverse Dzyaloshinsky—Moriya interaction as the microscopic mechanism of the magneto-electric coupling.

As the introduction of an antiferromagnetic exchange coupling J_2 between NNN spins in 1D-magnets results in a magnetically frustrated scenario, irrespective of an antiferro- or ferromagnetic coupling J_1 between NN spins, Bursill *et al.* [79] calculated the phase diagram for the 1D magnetic chain where the NN ferromagnetic coupling J_1 competes with the NNN antiferromagnetic coupling J_2 of the magnetic moments. As a result, the authors found long-range magnetic ordering with a helical arrangement of the ordered moments at zero temperature. If the ratio $|J_2/J_1| = \alpha$ is larger than a critical ratio $\alpha_c = 1/4$, the helix with a pitch angle $\theta = \arccos[1/(4\alpha)]$ between the orientations of adjacent magnetic moments is formed. This helix interpolates between the arrangement of a ferromagnetic chain ($0 \leq \alpha \leq \alpha_c$) and two decoupled antiferromagnetic chains ($\alpha \longrightarrow \infty$).

From neutron diffraction, long-range magnetic ordering in form of a spin helix with a propagation vector $\boldsymbol{Q} = (0, 0.53, 0)$ has been observed in $LiCuVO_4$ below $T_{\mathrm{N}} = 2.1$ K (Ref. [80]). This incommensurate magnetic order was characterized by Cu^{2+} moments that lie within the ab plane with a pitch angle close to 90° and an ordered moment of 0.31 μ_{B}. The dispersion of the magnetic excitations were measured by inelastic neutron scattering [81]. A detailed analysis

allowed the determination of the relevant exchange paths resulting in NN ferromagnetic exchange ($J_1/k_B = -19$ K), which is active via the two 90° Cu-O-Cu bonds, and NNN antiferromagnetic exchange ($J_2/k_B = 45$ K) acting via Cu-O-O-Cu superexchange paths, respectively. By using the quantum spin models [79], these parameters define a helical spin ground state with a pitch angle close to 90° as experimentally observed. A classical Hamiltonian would result in a much smaller pitch angle between neighbouring spins along the chain and, therefore, the fact of a pitch angle close to 90° has been taken as proof of the importance of quantum fluctuations in $LiCuVO_4$ (Ref. [81]).

The particular spin-helix ground state in $LiCuVO_4$ as a result of magnetic frustration between NN and NNN exchange interactions gave the motivation to start a closer inspection of the magnetic properties in the low-temperature range in order to establish the entire magnetic phase diagram (H, T). NMR spectra shed light on the impact of an increasing applied magnetic field H on the spin helix. The magnetic dipole field of one copper moment $\boldsymbol{\mu}$ at the probing nuclei is given by

$$\mathbf{H}_{\text{dipole}} = \frac{3 \cdot \boldsymbol{x}_{ijk}(\boldsymbol{x}_{ijk} \cdot \mu_{ijk,p})}{|x_{ijk}|^5} - \frac{\mu_{ijk,\phi}}{|x_{ijk}|^3}, \tag{4}$$

where the vector x_{ijk} points from the magnetic copper ion to the probing nuclear site. In case of lithium as the probing nucleus at $r = (a/4, b/4, c/4)$, this vector is indexed according to Fig. 1 in Ref. [82]:

$$\mathbf{x}_{ijk} = \mathbf{r} - \begin{pmatrix} a \\ 0 \\ 0 \end{pmatrix} \cdot i - \begin{pmatrix} 0 \\ b/2 \\ 0 \end{pmatrix} \cdot j - \begin{pmatrix} a/2 \\ 0 \\ c/2 \end{pmatrix} \cdot k. \tag{5}$$

In order to obtain quantitative results of the magnetic dipole field at the lithium nuclear site, Eq. 4 has to be scaled to 0.31 $\mu_B/(\sqrt{a^2 + b^2 + c^2})^3$. The crystal lattice constants are taken from [45] and 0.31 μ_B is the ordered moment found by neutron scattering [80]. The helical arrangement of the magnetic moments $\mu_{ijk,\phi}$ is parametrized as

$$\mu_{ijk,\phi} = \begin{pmatrix} \cos\left[\frac{\pi}{180^\circ}(83.6^\circ \cdot j + \phi \cdot 9)\right] \\ \sin\left[\frac{\pi}{180^\circ}(83.6^\circ \cdot j + \phi \cdot 9)\right] \\ 0 \end{pmatrix} \cdot (-1)^k, \tag{6}$$

where $(83.6 \pm 0.6)^\circ$ is the pitch angle of the ordered helix [81] which propagates along the crystallographic b-axis. This propagation along the b-axis is expressed by the use of the index j (cf. Eq. 5). The parameter $\phi = 0 \ldots 40$ accounts for all phases of the helix within $0^\circ \ldots 360^\circ$ and the factor $(-1)^k$ ensures that adjacent ab-planes are coupled antiferromagnetically along the c-axis. In order to obtain a simulation of the spectrum intensity $I(H)$ for each component of the dipole field of Cu^{2+} moments at the probing nuclear lithium site, the response of nuclear sites experiencing the same local field are contracted within a Lorentzian line

$$I(H) = \sum_{\phi=0}^{40} w^2/([H - H_{dipole}]^2 + w^2), \tag{7}$$

where the summation has to be calculated over all possible phases ϕ. A linewidth w of the nuclear spin ensembles which experience the same local field must be assumed. It is reasonable to take the value of the linewidth $w = 75$ Oe of the spectral lines in the paramagnetic phase. The plot of the simulated intensity $I(H)$ together with the experimental data is shown in Fig. 7 (left frame), which exhibits a nice congruence of simulation and experiment.

At elevated applied magnetic fields H, the ^{7}Li spectrum for H oriented parallel to the crystallographic b-axis exhibits also the pronounced double-horn shape which is characteristic for incommensurate magnetic order (see Fig. 7, middle frame). This observation suggests a spin-flop transition to take place, where the spin plane rotates to be perpendicular to the direction of the applied magnetic field H. Accordingly, the simulations of the ^{7}Li spectra (solid lines

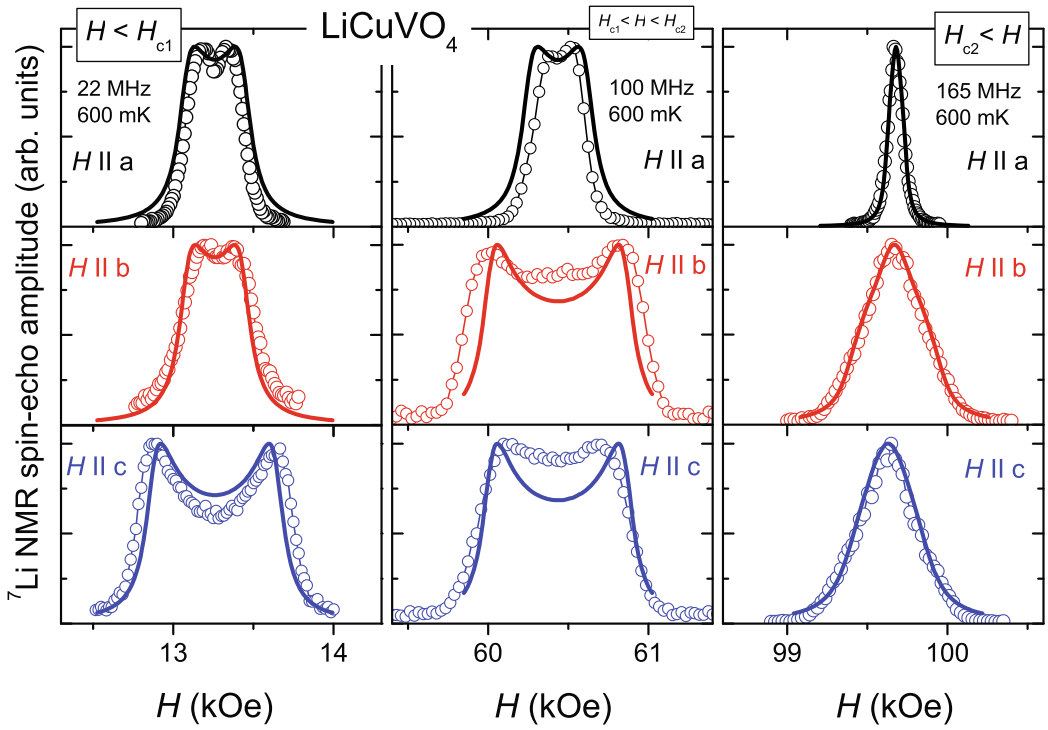

Fig. 7. ^{7}Li NMR spectra for externally applied magnetic fields $H < H_{c1} \approx 25$ kOe (left frame), $H_{c1} < H < H_{c2}$ (middle frame), and $H > H_{c2} = 75$ kOe (right frame) at 600 mK. The solid lines are simulations $I(H)$ of the magnetic dipole field $\mathbf{H}_{\rm dipole}$ of the magnetically ordered copper moments of $0.31\mu_{\rm B}$ at the probing ^{7}Li nuclear site.

in Fig. 7, middle frame) are obtained by choosing the coordinates of the helix structure as (cf. Eq. (6)):

$$\mu_{ijk,\phi} = \begin{pmatrix} 0 \\ \sin\left[\frac{\pi}{180^\circ}(83.6^\circ \cdot j + \phi \cdot 9)\right] \\ \cos\left[\frac{\pi}{180^\circ}(83.6^\circ \cdot j + \phi \cdot 9)\right] \end{pmatrix} \cdot (-1)^k, \quad \text{for } H \parallel a \quad \text{and} \tag{8}$$

$$\mu_{ijk,\phi} = \begin{pmatrix} \sin\left[\frac{\pi}{180^\circ}(83.6^\circ \cdot j + \phi \cdot 9)\right] \\ 0 \\ \cos\left[\frac{\pi}{180^\circ}(83.6^\circ \cdot j + \phi \cdot 9)\right] \end{pmatrix} \cdot (-1)^k, \quad \text{for } H \parallel b. \tag{9}$$

For the orientation $H \parallel c$, the situation described by Eq. 6 remains unchanged. AFMR experiments [83] and dielectric spectroscopy [84] determined this spin-flop transition to take place at the critical field $H_{c1} \approx 25$ kOe. For further increase of the applied magnetic field H, high-field magnetization measurements have shown that a magnetic field $H \approx 75$ kOe applied along the c-axis induces an anomaly in the derivative of the magnetization $M(H)$ [85] which was interpreted as a significant change of the incommensurate magnetic helix seen at low fields H. Indeed, the ^{7}Li NMR spectra obtained at applied magnetic fields $H > H_{c2} = 75$ kOe indicate a change of the dipole fields of the long-range ordered copper moments at the nuclear sites: in the right frame of Fig. 7 it is seen that a single unsplit line occurs for each orientation of the applied magnetic field $H \parallel a, b$, and c.

Summarizing the ^{7}Li NMR investigations concerning the magnetic structure of the ordered moments μ according to Eqs. 6, 8, and 9 for applied magnetic fields $H < H_{c2}$ one can see that the moments build a planar helix which is spanned by two orthogonal unit vectors $\mathbf{l_1}$ and $\mathbf{l_2}$.

Consequently, the normal unit vector $\mathbf{e} = \mathbf{l_1} \times \mathbf{l_2}$, which represents the helix axis, can be flipped by applying an external magnetic field H:

$$\begin{array}{c} H < H_{c1} : \mathbf{e} \parallel c\text{-axis} \\ H_{c1} < H < H_{c2} : \mathbf{e} \parallel H. \end{array} \tag{10}$$

In order to simulate the spectra for applied magnetic fields $H > H_{c2}$, one has to abandon the concept of a planar helical magnetic structure which is oriented according to $\mathbf{e} \parallel H$. The simulation of the unsplit spectra pattern (solid lines in the right frame of Fig. 7 for $H > H_{c2}$) is obtained by assuming a sinusoidal modulation of the magnetic moment component which is aligned along the direction of the applied magnetic field H [82]:

$$\mu_{ijk,\phi} = \begin{pmatrix} \cos\left[\frac{\pi}{180^\circ}(83.6^\circ \cdot j + \phi \cdot 9)\right] \\ 0 \\ 0 \end{pmatrix} \cdot (-1)^k, \quad \text{for } H \parallel a, \tag{11}$$

$$\mu_{ijk,\phi} = \begin{pmatrix} 0 \\ \cos\left[\frac{\pi}{180^\circ}(83.6^\circ \cdot j + \phi \cdot 9)\right] \\ 0 \end{pmatrix} \cdot (-1)^k, \quad \text{for } H \parallel b, \tag{12}$$

$$\mu_{ijk,\phi} = \begin{pmatrix} 0 \\ 0 \\ \cos\left[\frac{\pi}{180^\circ}(83.6^\circ \cdot j + \phi \cdot 9)\right] \end{pmatrix} \cdot (-1)^k, \quad \text{for } H \parallel c. \tag{13}$$

This implies that there are *no* orthogonal unit vectors $\mathbf{l_1}$ and $\mathbf{l_2}$ spanning a helix $\mathbf{e} = \mathbf{l_1} \times \mathbf{l_2}$. The magnetic structure at applied magnetic fields H higher than H_{c2} rather exhibits a sinusoidal modulation of the magnetic moment: it is a modulation of the collinear component of the ordered magnetic moment with respect to the direction of the applied magnetic field H. Accordingly, this collinear modulation for $H > H_{c2}$ can be described as a breakdown of the planar helix structure:

$$H_{c2} < H : \mathbf{l_1} \parallel H \quad \text{and} \quad \mathbf{l_2} = 0. \tag{14}$$

A recent theoretical investigation of the changing magnetic structures at H_{c2} identified a transition between the helix phase and a spin-density wave, the so called SDW_2 phase [86]. In that work, the experimentally observed spin modulated state in high fields $H > H_{c2}$ has been described by a density-wave order of bound magnon pairs. For very high fields near the saturation field, these spin-density waves are expected to be replaced by spin nematic phases which are characterized by the condensation of bound multi-magnons [86]. From measurements of different physical properties (heat capacity, NMR, and AFMR) there was obtained an intermediate phase which separates the paramagnetic phase and the long-range ordered phase below around 2.3 K (cf. Fig. 8): in addition to the anomaly at the transition into the magnetically ordered phase at $T_N = 2.3$ K, the temperature dependence of the specific heat capacity C/T exhibits a clear lambda-type anomaly at $T = 10$ K for an applied magnetic field $H = 90$ kOe along the crystallographic c-axis (upper frame in Fig. 8). Concomitantly, the linewidth Δ_{NMR} starts to increase drastically toward lower temperatures for $T < 10$ K (middle frame in Fig. 8) and AFMR measurements extrapolated to zero applied magnetic fields $H = 0$ kOe yield the opening of an excitation gap toward lower temperatures for $T < 10$ K (lower frame in Fig. 8). The nature of this intermediate phase is not clear yet, but probably a short-range magnetic order is indicated for temperatures $2.3 < T < 10$ K in $LiCuVO_4$.

In addition to the magnetic properties described above, $LiCuVO_4$ turned out to be a prototypical example of a multiferroic compound where electric polarization P is induced by the magnetically ordered structure of the planar spin helix [84]. The magnetoelectric properties meet exactly the theoretical prediction $P \propto [\mathbf{e} \times \mathbf{Q}]$ (Ref. [87]), where $\mathbf{e} = \mathbf{l_1} \times \mathbf{l_2}$ is the vector orthogonal to the spin helix plane (cf. Eq. 10) and $\mathbf{Q}$ is the wave vector of the helix, which propagates along the crystallographic b-axis. The results of our magnetic and dielectric measurements are summarized in the phase diagram of figure 9. Measurements of the pyroelectric

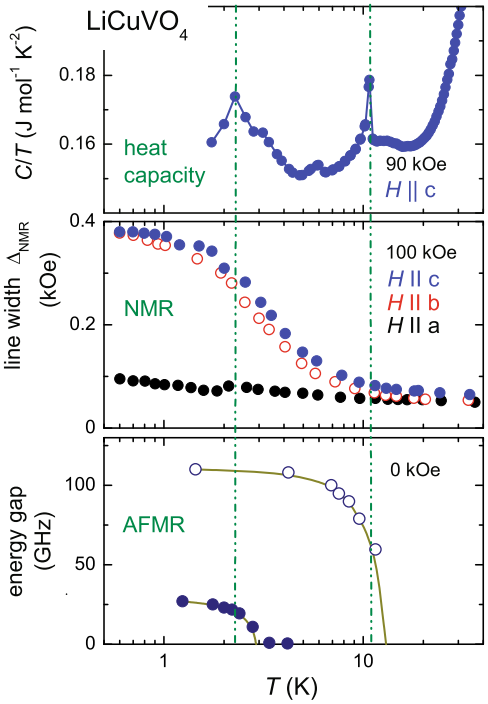

Fig. 8. Temperature dependences of heat capacity, NMR, and AFMR indicating two phase transitions around 2.3 and 10 K (dashed vertical lines) in $LiCuVO_4$. Applied magnetic fields are 0, 90, and 100 kOe, respectively. The solid lines in the lower frame are drawn to guide the eye.

and magnetoelectric currents revealed a considerable anisotropy of the electric polarization where the absolute value of P strongly depends on the particular plane of the spin helix. This anisotropy is consistent with recent theoretical predictions [88], which are based on density functional calculations. Due to the ability to switch the direction of the ab helix in the helical spin-ordered state at $H_{c1} < H < H_{c2}$, $LiCuVO_4$ is ideally suited to test the theoretically predicted symmetry relations for multiferroic helical magnets [87–89].

Oscillations of the spin-spin relaxation T_2

The presence of small static electric or magnetic fields either internal or external at the nuclear site leads to a modulation of the spin-echo intensity [90]. The occurrence of such harmonic oscillations in the time evolution of the nuclear transverse magnetization $M_{x,y}(t)$ provides an access to very weak interactions between the probing nuclei and their surroundings which are too weak to produce a splitting of the NMR spectral lines in a static experiment. An enumeration of several examples for such interactions is given by the JI_1I_2 coupling in organic molecules [91] via indirect dipolar coupling mediated by induced electron magnetic moments, the JI_1I_2 coupling in metals [92] via indirect dipolar coupling mediated by conduction electrons (Ruderman-Kittel interaction), and the electric quadrupole coupling between the nuclear quadrupole moment Q and the surrounding electric field gradient (EFG) [93,94]. In the case of the antiferromagnetic parent compound $YBa_2Cu_3O_{6.05}$ (T_N = 415 K) of the high-temperature superconductors it was shown that the modulation frequency ν of the spin-echo intensity measures the sublattice magnetization of the in-plane copper moments Cu(2) (Ref. [95]). For this purpose, the modulation frequency ν was converted into internal magnetic field values $\nu = (^{137}\gamma/2\pi)B_{int}$, with $^{137}\gamma$ being the gyromagnetic ratio of the probing barium nuclei ^{137}Ba. The temperature dependence of this sublattice magnetization could be explained in terms of a spin-wave model for quasi-two-dimensional antiferromagnets.

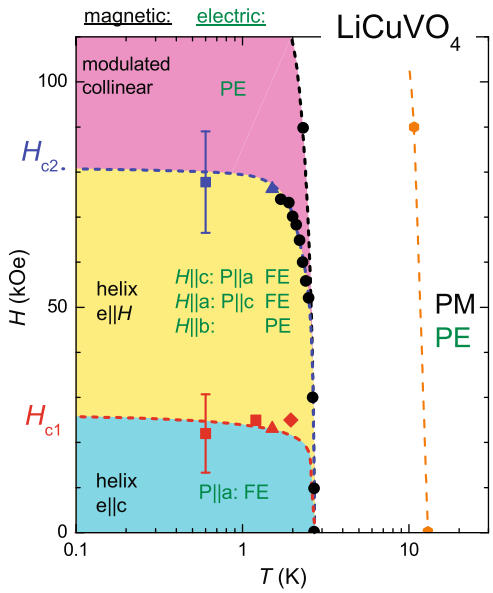

Fig. 9. Phase diagram (H, T) of $LiCuVO_4$. The magnetic (left column) and electric (right column) states document the multiferroicity of $LiCuVO_4$ [84]. Abbreviations denote the PM (paramagnetic), PE (paraelectric), and FE (ferroelectric) phases, respectively. The orange dashed line represents the experimental results of Fig. 8 for an intermediate phase within the temperature range $2.3 < T < 10$ K.

Quantitative analyses in those cases, where the electric quadrupole coupling between the nuclear quadrupole moment Q and the surrounding EFG yields the spin-echo modulation, are given in [94,96,97]. The time dependent nuclear transverse magnetization $M_{x,y}(t)$ consists of a monotonically decaying spin-echo amplitude with a superimposed oscillatory component:

$$M_{x,y}(2\tau) = \exp\left[-\frac{2\tau}{T_2}\right] \cdot [C_0 + C_1 \cdot \cos(2a\tau + \delta_1) + \dots],$$

where C_0, C_1, and δ_1 are constants. The quadrupole coupling constant $eV_{zz}Q/h$ is obtained from the oscillation frequency $2a = [3eV_{zz}Q/4\hbar I(2I-1)](3\cos^2\theta - 1)$ (Ref. [97]). With the usual abbreviation for the quadrupole frequency $\nu_Q = 3eV_{zz}Q/[2\hbar I(2I-1)]$, the oscillation frequency reduces to $2a = (\nu_Q/2) \cdot (3\cos^2\theta - 1)$. A modification of $M_{x,y}(2\tau)$ has been introduced by [95], which accounts for the exponential damping of the oscillations amplitude: in that work, the amplitude of the oscillating term has been replaced by an exponential term $C_1\exp(-\lambda \cdot \tau)$ which arises from a distribution of asymmetry parameters η because of structural disorder. Accordingly, the spin-echo modulation in $LiCuVO_4$ was best fitted with the following formula (solid lines in Fig. 10):

$$M_{x,y}(2\tau) = \exp\left[-\frac{1}{2}\left(\frac{2\tau}{T_{2G}}\right)^2\right] \cdot [C_0 + C_1\exp(-\lambda \cdot \tau) \cdot \cos(2\pi\nu \cdot \tau + \delta_1)] + \text{const.} \qquad (15)$$

The first term gives the usual spin-spin relaxation rate $1/T_{2G}$ (the particular Gaussian form of the spin-spin dephasing process was first established by Pennington *et al.* for the cuprate superconductors, where an indirect coupling between the nuclear spins is mediated by the antiferromagnetic fluctuations of the electron spins in the CuO_2 planes [98]). This so called Gaussian decay turned out to be also the proper description for the ^{7}Li spin-spin relaxation in $LiCuVO_4$ (Ref. [58]).

The measurements of the oscillating spin-echo decay in Fig. 10 were performed at an irradiation frequency of 165 MHz, which corresponds to applied magnetic fields near to $H = 100$ kOe. For $H = 100$ kOe, a transition from the paramagnetic state into the modulated collinear ordered

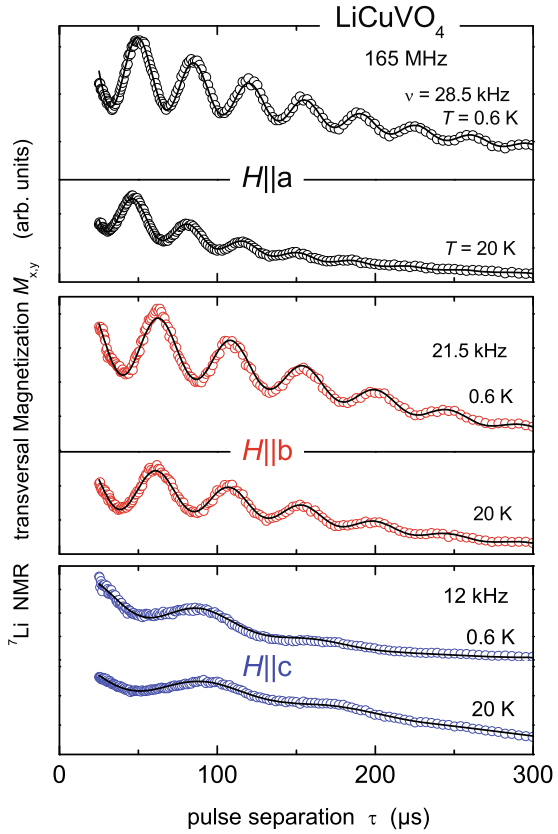

Fig. 10. Spin-spin relaxation of the transversal magnetization $M_{x,y}$ of $LiCuVO_4$ in the paramagnetic ($T = 20$ K) and AFM ordered ($T = 0.6$ K) state. The irradiation frequency of 165 MHz corresponds to an applied magentic field $H = 100$ kOe. Solid lines are fits to Eq. 15.

structure at T_N takes place according to the phase diagram in figure 9. With H being oriented along each crystal axes a, b, and c, the oscillation frequency and, hence, the EFG has been measured in the paramagnetic ($T = 20$ K) and magnetically ordered AFM state ($T = 0.6$ K). Within the experimental error, there is no change of the oscillation frequency ν between the paramagnetic and modulated collinear state. Accordingly, there is also no change of the EFG in the modulated collinear state which might depict the paraelectricity of $LiCuVO_4$ for this state. Probably, the magnetically induced redistribution of electron charges in multiferroic compounds yields changes of the local EFG and, hence, might be detectable via the effect of an oscillating spin-echo decay.

4.2 Tuning the spin gap

This section is devoted to the spin-gap ground states of quantum-spin chains apart from long-range magnetic order. A spin-gap magnet can be doped in different ways: using diamagnetic or paramagnetic impurities, substituting on the site of a magnetic or a nonmagnetic ion, and with the substitution being isovalent or not. In $Na_{1-x}Li_xV_2O_5$ the isovalent substitution of Na^+ by the smaller Li^+ ion results in a local distortion of the lattice and perturbation of the exchange interaction between the electrons on the vanadium ladders but does not change the number of electrons on the ladders. Substitution of Ca^{2+} instead of monovalent Na^+ in $Na_{1-x}Ca_xV_2O_5$ induces additional electrons into the vanadium ladders. In $Cu_{1-x}Mg_xGeO_3$ the nonmagnetic Mg^{2+} ions break the Cu^{2+} spin $S = 1/2$ chains, whereas in $Cu_{1-x}Ni_xGeO_3$ the magnetic spins of Ni^{2+} ions ($S = 1$) locally enhance the magnetization of the copper chains.

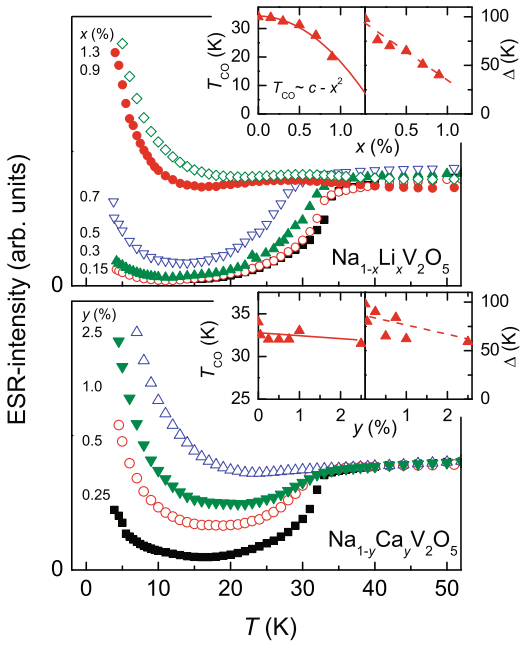

Fig. 11. Temperature dependence of ESR intensity, i.e. spin susceptibility χ_{ESR} in NaV_2O_5 doped with Li (upper frame) and Ca (lower frame). Insets: Dependence of transition temperature T_{CO} and energy gap $\Delta(0)$ at zero temperature on the impurity concentration.

To introduce some general aspects, Fig. 11 illustrates the low-temperature susceptibility determined from the ESR intensity in NaV_2O_5 doped by Li and Ca. The spin susceptibility above the charge-order transition is nearly insensitive to the doping. However, below the transition one observes a Curie-like increase of the susceptibility that increases with doping. This is the fingerprint of the paramagnetic centers induced by the impurities. In the samples with $x = 1.3\%$ Li doping as well as with $y = 2.5\%$ Ca doping the transition is no longer visible, but no magnetic order is observed down to the lowest experimental temperature of 1.5 K. The analysis of the data is described in detail in Ref. [99]: a Curie law $\propto 1/T$ was fitted to the data points below 10 K and subtracted. Then the resulting curves were analyzed using a mean-field-like temperature dependence of the energy gap $\Delta(T)$ and $\chi(T) \propto \exp(-\Delta(T)/k_{\mathrm{B}}T)$ with only two fit parameters, i.e. the gap value at zero temperature $\Delta(0)$ and the transition temperature T_{CO}. The results are displayed in the insets of figure 11. For Li doping the transition temperature strongly decreases with an approximately quadratic law, whereas the transition temperature is only weakly shifted for Ca doping. In both cases the energy gap varies linearly with the impurity content, but again the decrease is weaker for Ca than for Li substitution. Interestingly, the ratio $2\Delta/k_{\mathrm{B}}T_{\mathrm{CO}}$ decreases with increasing doping from the strong coupling value of about 6 in undoped NaV_2O_5 to values close to the mean-field result of 3.53.

The stronger influence of Li doping as compared to Ca is probably due to the different ionic radii of both dopants: The ionic radius of Li^+ is about 40% smaller than that of Na^+ whereas Ca^{2+} and Na^+ have comparable radii. Thus, Li doping locally distorts the lattice and, hence, breaks the spin dimerization. Ca doping on the other hand does not disturb the lattice, but adds one more electron to the vanadium sites, which locally polarizes the dimerized background. In addition the very small mass of the Li ions in comparison with the Na ions may be of importance: in a normal spin-Peierls system the transition depends on the spin-phonon coupling g_{sp} and the phonon frequency ν_{p} [100]. The transition temperature should be of the order of $g_{\mathrm{sp}}/\nu_{\mathrm{p}}^2$. Substitution of the lighter lithium ions for sodium is expected to increase the phonon frequency ν_{p}, thus reducing the transition temperature in addition to the influence of disorder, which anyway gradually suppresses the phase transition. This scenario could explain the faster decrease of the transition temperature upon Li-doping as compared to Ca doping.

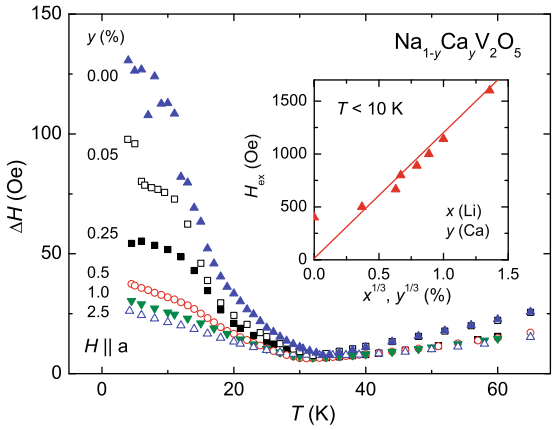

Fig. 12. Temperature dependence of the linewidth in $Na_{1-y}Ca_yV_2O_5$ below 70 K for Ca concentrations $0 \leq y \leq 2.5\%$. Insets: Defect-concentration dependence of the effective exchange field H_{ex} between the defects determined from the low-temperature linewidth.

Further information on the paramagnetic centers generated by the doping is obtained from linewidth and resonance field. Like the spin susceptibility, g value and linewidth above the transition were found to be nearly independent of the impurity concentration. Below the transition the overall anisotropy of the g tensor remains unchanged, only slight shifts less than 0.3% occur. This proves that the impurity induced spin objects reside on the vanadium sites. Figure 12 shows the evolution of the linewidth at low temperatures with increasing Ca concentration, which is very similar to the case of Li doping. In pure NaV_2O_5 below T_{CO} the linewidth increases with decreasing temperature from about 10 Oe up to approximately 120 Oe (250...400 Oe, dependent on the sample) for the magnetic field applied perpendicular (parallel) to the crystallographic c axis, approaching saturation at about 8 K. With increasing impurity concentration the low-temperature saturation value strongly decreases. Detailed experiments have proven the low-temperature linewidth to be independent of the microwave frequency in the investigated range from 9 to 75 GHz.

The reason for this line broadening is the weakening of the exchange narrowing between the residual spins on dimerization of the majority of spins below the transition. In the pure sample less than 0.1% defects remain on vanadium sites with nearly negligible exchange between them. In principle one expects a hyperfine splitting of the spectra due to the ^{51}V nuclear spin $I = 7/2$. However, no splitting is observed down to 1.5 K, except for very pure undoped singe crystals, where indications of a substructure have been reported [101]. The situation is somehow similar to the case of $Na_{0.01}V_2O_5$, where the electrons induced by the Na^+ ions into the diamagnetic V_2O_5 lattice are not localized at a certain vanadium site, but are distributed over $N = 4$ vanadium sites [102]. This has been deduced from the hyperfine structure in that compound which is resolved in $2NI + 1 = 29$ lines at 130 K, but is smeared out at low temperature due to inhomogeneous broadening effects. The overall low-temperature linewidth and its anisotropy observed in NaV_2O_5 are in good agreement with the inhomogeneous width expected from the anisotropic hyperfine interaction ($A_{\|} = 190$ Oe and $A_{\|}/A_{\perp} = 2$) [103]. In NaV_2O_5 the defects can be imagined to polarize the neighbouring spins in the dimerized matrix antiferromagnetically and, hence, generate multi-spin clusters, which involve several vanadium sites, where the hyperfine splitting is smeared out, in contrast to a single V^{4+} ion, where the $3d^1$ electron interacts with only one nuclear spin.

The decrease of the low-temperature linewidth on increasing doping allows to estimate the effective exchange field between the defects using the expression for the exchange narrowed linewidth with the second moment due to the hyperfine interaction. The result is depicted in the inset of figure 12. The exchange field increases linearly with the cubic root of the impurity concentration corresponding to the average distance between two defects. The value of about $H_{ex} \approx 1.5$ kOe corresponding to an effective exchange constant $J_{ex}/k_B = 0.1$ K reached at

2.5% impurity concentration is probably too small to induce antiferromagnetic order. Magnetic frustration has been suggested as another reason for the non-existence of antiferromagnetic order in NaV_2O_5 (Ref. [104]). A similar situation was observed in the spin $S = 1$ Haldane system Y_2BaNiO_5, where also the Curie contribution to the susceptibility increases with, e.g., Zn doping on the Ni site without any indication of magnetic order at low temperatures [105]. Only if the system is intrinsically near a magnetic instability, small doping is enough to induce magnetic order [106,107]. This is the case, e.g., in the spin-Peierls system $CuGeO_3$ and in the Haldane system $PbNi_2V_2O_8$.

4.3 Formation of multi-spin clusters

But before the peculiarities of the impurity-induced ordering in spin-gap systems will be considered, the properties of the paramagnetic defect centers have to be discussed. Interestingly, in the case of small doping amounts, the peculiar nature of the impurity is not so decisive for its effect on the ground state, as just presented for NaV_2O_5 and also well documented in literature for $CuGeO_3$: in that case both Mg and Ni substituted on Cu sites in concentrations up to $x = 3\%$ as well as Si doped onto the Ge site up to $x = 1\%$ result in a linear decrease of the spin-Peierls transition temperature with increasing x and the appearance of an antiferromagnetic phase at lower temperatures [108]. The observed universality can be explained in terms of a model considering local moments released by the impurities and randomly distributed inside the gapped singlet background [109].

If impurities are embedded into a spin-gap magnet, additional magnetic degrees of freedom appear on the singlet background, which give rise to a low-temperature contribution to the magnetic susceptibility. It has been shown that both in spin-Peierls and Haldane systems breaking the spin chains locally destroys the singlet state [110–112]: on both sides of a diamagnetic impurity multi-spin clusters with a local staggered magnetization occur. The local staggered magnetization decays exponentially with increasing distance from the impurity. A similar effect appears in the case of a magnetic impurity of different spin value in the chain. Even diamagnetic impurities, doped on other sites than in the chain, locally break the dimerization via chemical pressure, giving rise to comparable multi-spin objects, as indicated by the low-temperature spectra in doped NaV_2O_5.

These multi-spin clusters carry a net spin and a net magnetic moment. For a broken dimerized $S = 1/2$ chain the net spin value of such a cluster is obviously $1/2$. Interestingly, breaking of spin $S = 1$ chains is theoretically expected to result in effective $S = 1/2$ degrees of freedom at the ends of the chain segments as well [113]. ESR experiments confirmed the multi-spin nature of the magnetic defects created by impurities in the spin-Peierls magnet $CuGeO_3$ [114,115]. Indications of $S = 1/2$ degrees of freedom were found in ESR spectra of impurities in the Haldane systems NENP (Ref. [113,116]) and Y_2BaNiO_5 (Ref. [117]), but also doubts arose from specific-heat measurements [118].

Temperature dependent ESR experiments in pure and Mg doped $PbNi_2V_2O_8$ corroborate the spin $S = 1/2$ character of the chain defects. Figure 13 shows the evolution of the ESR spectra in the pure system. The structure of $PbNi_2V_2O_8$ is isomorphous to $SrNi_2V_2O_8$ (Ref. [119]), which crystallizes in a tetragonal structure (space group $I4_1cd$), where slightly distorted NiO_6 octahedra are edge-shared around the fourfold screw axis along the c direction, thus, forming one-dimensional $S = 1$ chains. At high temperatures the spectrum consists of a single exchange narrowed resonance line at $g = 2.2$, typical for Ni^{2+}. The main source of broadening at high temperatures is the zero-field splitting of the $S = 1$ state due to the crystal field in the distorted NiO_6 octahedra. Using Eq. 3 with the intra-chain exchange constant $J/k_B = 95$ K derived from the magnetic susceptibility [119] and the experimental linewidth of about $\Delta H_\infty \approx 2.5$ kOe yields a zero-field splitting parameter $D_{ZFS}/k_B \sim 5$ K. This is in agreement with the values derived from the spin-excitation spectrum: $D_{ZFS} = -0.23$ meV [119] and $D_{ZFS} = -0.45$ meV [106]. The discrepancy between these two values is due to different models of the magnetic interactions used for the data analysis.

On lowering the temperature below the Haldane gap ($\Delta/k_B \approx 40$ K (Ref. [119])), the line first strongly broadens and then splits into two components, one of which resides at $g = 2.2$ and

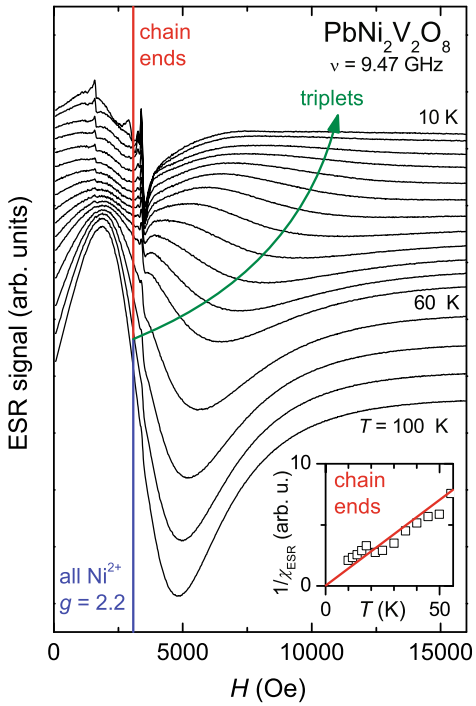

Fig. 13. Temperature evolution of the ESR spectra in $PbNi_2V_2O_8$: Starting at 10 K, 12 K, 16 K, in 5 K steps below 60 K and 10 K steps above. Inset: inverse ESR intensity of the line at $g = 2.2$ at low temperatures. The solid line indicates a Curie law.

the other one shifts to high fields. The intensity of the high-field component decreases toward low temperatures indicating the thermal activation of the corresponding spins, the low-field line follows a Curie law. Including experiments at higher frequencies [120], the high-field line can be explained by thermal triplet $S = 1$ excitations with a zero-field splitting of $D/k_B \approx 4$ K, comparable to the value obtained from the high-temperature linewidth. The low-field line does not show any indication for a zero-field splitting, which would be characteristic for a spin larger than 1/2. The effect of the single-ion anisotropy on the energy spectrum of the end of the Haldane chain was analyzed in Ref. [121], where it was shown that the D-term does not affect the central peak frequency of the ESR spectrum of long spin-chain segments. This is consistent with the concept of an effective spin $S = 1/2$ and, therefore, the line at $g = 2.2$ is ascribed to the chain ends. This impurity-induced line strongly increases on doping where it dominates the ESR signal at low temperatures, confirming the $S = 1/2$ character of the multi-spin clusters in $Pb(Ni_{1-x}Mg_x)_2V_2O_8$ as well.

4.4 Coexistence of paramagnetic and antiferromagnetic phases

Having established the general character of the multi-spin objects in spin-Peierls and Haldane chains as chain segments with a locally staggered magnetization and an effective spin $S = 1/2$, now the impurity induced magnetic order in Mg doped $CuGeO_3$ and $PbNi_2V_2O_8$ shall be compared. In $Cu_{1-x}Mg_xGeO_3$, the spin-Peierls temperature decreases from 14 K at $x = 0$ to about 10 K at $x_c = 0.023$ where the transition abruptly disappears. Concomitantly, for $0 \leq x \leq 0.023$ a dimerized antiferromagnetic phase develops with the Néel temperature linearly increasing from zero up to 3.4 K at x_c, where it abruptly jumps to 4.2 K. For $x \geq x_c$ a uniform antiferromagnetic phase develops, with the Néel temperature approximately constant at about 4.2 K up to $x = 0.04$ and again gradually decreasing for larger x. The discontinuity at x_c has been identified as a first-order phase transition [122]. Detailed ESR experiments

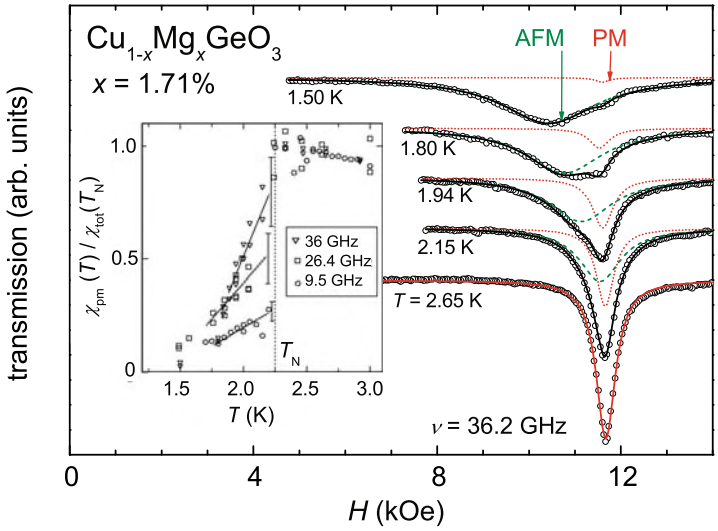

Fig. 14. Temperature evolution of the ESR spectra of $CuGeO_3$ doped with 1.71% Mg below 3 K at 36 GHz. The fit curves (solid) are decomposed in paramagnetic (PM) and antiferromagnetic (AFM) fraction. Inset: Temperature dependence of the intensity of the PM fraction normalized to the full intensity at T_N.

revealed the coexistence of paramagnetic (PM) and antiferromagnetic (AFM) modes for $x < 0.04$ below T_N, indicating a separation in paramagnetic and antiferromagnetic phases [124]. In $Pb(Ni_{1-x}Mg_x)_2V_2O_8$ antiferromagnetic order appears in a similar way like in $CuGeO_3$ (but without any discontinuity) with T_N monotonously increasing from zero up to 3.4 K at $x = 0.04$ and remaining unchanged for higher doping concentrations under consideration (up to $x = 0.12$) [119]. Again, for small concentrations $x < 0.02$ a coexistence of paramagnetic and antiferromagnetic resonances is found [123].

Thus, in both spin-gap systems one observes some kind of phase separation for low doping levels. Figure 14 summarizes exemplarily the experimental results of $CuGeO_3$ doped with 1.71% Mg. Above T_N the ESR signal consists of a single Lorentzian line at $g \approx 2.3$, which originates from the spin-1/2 defects on the spin-gap background. For $T \leq T_N$ the line splits into two components, one of which broadens and shifts to lower resonance fields. The other component resides at the paramagnetic resonance field, but looses intensity with decreasing temperature. The frequency/field dependence and the anisotropy of the former line has been explained as antiferromagnetic resonance from long-range ordered regions in the sample, whereas the latter signal is ascribed to paramagnetic regions [124]. Comparing the intensity of the paramagnetic line for different frequency, i.e. different paramagnetic resonance field, at temperatures slightly below the phase transition, its fraction increases with increasing field, indicating a relative increase of the paramagnetic regions driven by the magnetic field.

The observed phase separation can be explained to result from the high inhomogeneity of the ordered phase, because the staggered magnetization induced by an impurity is localized on a short distance. Considering the spatial inhomogeneity, it means that the order parameter varies in space between a maximum value and zero. Consequently, a real microscopic phase separation into AFM and PM phases occurs. For nonzero temperature, AFM areas of different size embedded in the spin-gap matrix are expected [124]. Accordingly, macroscopic AFM regions provide AFM resonance and susceptibility. Small AFM clusters, i.e. isolated chain fragments, provide PM resonance signals and a Curie-like susceptibility. The numerical simulation [125] confirmed a strongly inhomogeneous ground state with practically 100% spatial modulation of the order parameter, implying a phase separation at a finite temperature.

At finite temperature the antiferromagnetic correlation of an impurity-induced multi-spin cluster with effective spin $S = 1/2$ vanishes on a distance L from the impurity atom estimated by the balance $JS^2 \exp(-2L/\xi) \sim k_B T$ of exchange and thermal energy, where J and ξ denote

the exchange constant and magnetic correlation length along a certain direction, respectively. On decreasing temperature the clusters increase in size L and begin to overlap, yielding areas of coherent antiferromagnetic order giving rise to the AFM resonance, whereas the PM line, which originates from single clusters, looses intensity. Application of an external magnetic field tries to align all spin-objects parallel and, thus, competes with the antiferromagnetic exchange interaction between the clusters. The field for breaking up the long-range order can be estimated correspondingly via $g\mu_{\mathrm{B}}H \sim JS^2 \exp(-2L/\xi)$. Thus, the ratio of paramagnetic and antiferromagnetic phases is easily controlled by a magnetic field.

Such kind of impurity-induced ordering on a spin-gap background provides an unconventional kind of microscopic phase separation. Usually phase separation is intensively studied in conducting materials, in manganites with the electronic phase separation into ferromagnetic droplets and antiferromagnetic regions (see, e.g., [126]), and in the context of stripe formation of the electron density in high-temperature superconductors [127] as paramount examples. These examples come along with a redistribution of charge-carrier density. But the phase separation in a doped spin-gap magnet takes place on a perfect dielectric background. Here the phase separation results from the interplay of the basic singlet background and nanoscopic AFM areas restored at impurity sites.

5 Summary

The best realization of a uniform 1D quantum spin chain (Cu^{2+}, $S = 1/2$), for which Bethe provided an exact solution of the Heisenberg model, is found among the phosphate compounds with $Sr_2Cu(PO_4)_2$. Due to its minor inter-chain interactions, this compound provides a record temperature range which is solely dominated by intra-chain properties. In addition, the local magnetic fields and electron fluctuations, which are probed by the NMR line shift K and nuclear spin-lattice relaxation rate $1/T_1$, respectively, exhibit temperature dependences which cannot be reconciled with theoretical predictions based on the analytical solution by the Bethe-ansatz: the low-temperature regime of $K(T)$ and the high-temperature regime of $1/T_1(T)$ exhibit approximately thermally activated behaviours, which suggest gap-like excitations. Indeed, in the presence of Dzyaloshinskii-Moriya (DM) interactions between magnetic moments, the opening of a gap in the magnetic excitation spectrum is expected, if the external field of the NMR experiment is applied parallel to the DM-vector. Therefore, the role of DM interaction in the phosphate compounds with their particular arrangement of isolated CuO_4 plaquettes remains as a future problem for theoretical and experimental studies.

The outstanding 1D magnetic properties of these phosphate compounds with isolated CuO_4 plaquettes are due to the vanishingly small intra-chain coupling of next-nearest neighbouring copper spins. As soon as this intra-chain coupling becomes appreciable, magnetic frustration occurs, if the next-nearest neighbouring spins are coupled antiferromagnetically. In this case, irrespective of the nearest-neighbour interaction to be FM or AFM, there is no spin configuration that simultaneously satisfies all of the interactions between the spins. A paradigm compound of such a magnetically frustrated 1D spin chain is $LiCuVO_4$ due to the edge-sharing geometry of CuO_4 plaquettes, which are lined up along the crystallographic b axis. The NMR spectra measurements confirm the helical spin structure in zero magnetic field, which was found by neutron-diffraction measurements. In addition, the simulation of the magnetic dipole fields of the copper moments at the probing nuclear site revealed a spin-flop transition around applied magnetic fields of 25 kOe: the plane of the helical spin structure is flipped with its vector aligned parallel to the orientation of the applied magnetic field. Concomitantly, the dielectric polarization in $LiCuVO_4$, induced by the incommensurate ordering of the helix, is flipped as well. This characterizes $LiCuVO_4$ as a multiferroic compound with strong magneto-electric coupling. The observed anisotropy of the absolute values of the dielectric polarization along different crystallographic axes strongly supports the theoretical concept which is based on the spin-orbit coupling at the copper site inducing an asymmetric electron-density distribution around the oxygen anions. This theory goes without displacements of oxygen anions from their centrosymmetric positions. In future, NMR studies of the electric field gradients via nuclear quadrupole interaction are expected to corroborate the present picture.

Systematic ESR investigations of prototypical quasi-1D compounds, as there are $LiCuVO_4$, $CuGeO_3$, and NaV_2O_5, revealed a universal temperature dependence of the linewidth – similar to that observed in the NMR spin-lattice relaxation rate – which was identified to be due to the symmetric part of the anisotropic exchange interaction. On the basis of the presented microscopic model the magnitude of the exchange parameters as well as their changes on approaching the phase transition are determined. These changes of the exchange parameters are directly related to fluctuations, e.g., of the lattice above the spin-Peierls transition in $CuGeO_3$ or of the electronic occupation of the vanadium sites above the charge-order in NaV_2O_5. Moreover, each of the systems considered allows to study quantitatively quantum effects peculiar to low-dimensional materials: effects of quantum interference in the ribbons of $LiCuVO_4$, interchain exchange in $CuGeO_3$, and the anisotropic ring-exchange processes in NaV_2O_5. Having established the universal relaxation behavior due to symmetric anisotropic exchange in prototypical spin-chains presented above enables to study more complex systems. An advanced application of this knowledge is given by the related 1D conductor β-$Na_{1/3}V_2O_5$, where the electronic occupation and charge-order pattern could be successfully derived from the ESR data. The 1D perovskite $KCuF_3$ turned out to be an exception: although the temperature dependence seems to follow the universal behavior indicative for symmetric anisotropic exchange it is impossible to describe its anisotropy in terms of this interaction. The solution is found in terms of a dynamical DM interaction due to a certain phonon mode, which becomes activated with increasing temperature.

Doping magnetic or non-magnetic impurities into spin-gap systems is another important topic, where ESR contributes valuable information. Here the influence of Li and Ca doping on the spin gap in NaV_2O_5 and the impurity induced antiferromagnetic order in the spin-Peierls system $CuGeO_3$ and the Haldane chain $PbNi_2V_2O_8$ have been discussed. A central result is the phase separation in $CuGeO_3$:Mg, which appears on a perfectly dielectric background. The induced antiferromagnetic order is highly inhomogeneous and, thus, coexists with paramagnetic regions. Their relative ratio can be controlled by means of an external magnetic field.

The above investigated examples of quantum spin chains reveal a complex interplay of spins, orbital moments, and charge as well as their coupling to the lattice. As local probes of these degrees of freedom, nuclear-spin resonance and electron-spin resonance turned out to be indispensable tools for the microscopic investigation of quantum effects in low-dimensional magnets.

This work was supported by the DFG via the Sonderforschungsbereich SFB 484 (Augsburg) and partly within Forschergruppe 960 (Augsburg, Dresden, Göttingen, Karlsruhe, Köln, München).

References

1. H. Bethe, Z. Phys. **71**, 205 (1931)
2. L. Onsager, Phys. Rev. **65**, 117 (1944)
3. R.E. Dietz, F.R. Merrit, R. Dingle, D. Hone, B.G. Silbernagel, P.M. Richards, Phys. Rev. Lett. **26**, 1186 (1971)
4. H. Benner, J. Wiese, Physica B **96**, 216 (1979)
5. H. Benner, J.P. Boucher, in *Magnetic Properties of Layered Transition Metal Compounds* (Kluwer Academic Publishers, Dordrecht, Boston, London, 1990), p. 323
6. M. Hase, I. Terasaki, K. Uchinokura, Phys. Rev. Lett. **70**, 3651 (1993)
7. A. Seidel, C.A. Marianetti, F.C. Chou, G. Ceder, P.A. Lee, Phys. Rev. B **67**, 020405(R) (2003)
8. S.A. Carter, B. Batlogg, R.J. Cava, J.J. Krajewski, W.F. Peck, Jr., T.M. Rice, Phys. Rev. Lett. **77**, 1378 (1996)
9. M. Isobe, Y. Ueda, J. Phys. Soc. Jpn. **65**, 1178 (1996)
10. M.D. Johannes, J. Richter, S.-L. Drechsler, H. Rosner, Phys. Rev. B **74**, 174435 (2006)
11. S.-L. Drechsler, O. Volkova, A.N. Vasiliev, N. Tristan, J. Richter, M. Schmitt, H. Rosner, J. Málek, R. Klingeler, A.A. Zvyagin, B. Büchner, Phys. Rev. Lett. **98**, 077202 (2007)
12. S.-L. Drechsler, J. Richter, R. Kuzian, J. Málek, N. Tristan, B. Büchner, A.S. Moskvin, A.A. Gippius, A. Vasiliev, O. Volkova, A. Prokofiev, H. Rakoto, J.-M. Broto, W. Schnelle, M. Schmitt, A. Ormeci, C. Loison, H. Rosner, J. Magn. Magn. Mater. **290-291**, 345 (2005)

13. D.C. Johnston, R.K. Kremer, M. Troyer, X. Wang, A. Klümper, S.L. Bud'ko, A.F. Panchula, P.C. Canfield, Phys. Rev. B **61**, 9558 (2000)
14. R. Nath, A.V. Mahajan, N. Büttgen, C. Kegler, A. Loidl, J. Bobroff, Phys. Rev. B **71**, 174436 (2005)
15. N. Motoyama, H. Eisaki, S. Uchida, Phys. Rev. Lett. **76**, 3212 (1996)
16. S. Salunke, M.A.H. Ahsan, R. Nath, A.V. Mahajan, I. Dasgupta, Phys. Rev. B **76**, 085104 (2007)
17. H. Rosner, H. Eschrig, R. Hayn, S.-L. Drechsler, J. Málek, Phys. Rev. B **56**, 3402 (1997)
18. R. Nath, Deepa Kasinathan, H. Rosner, M. Baenitz, C. Geibel, Phys. Rev. B **77**, 134451 (2008)
19. S. Eggert, I. Affleck, M. Takahashi, Phys. Rev. Lett. **73**, 332 (1994)
20. S.A. Zvyagin, A.K. Kolezhuk, J. Krzystek, R. Feyerherm, Phys. Rev. Lett. **93**, 027201 (2004)
21. A.U.B. Wolter, P. Wzietek, D. Jérome, S. Süllow, F.J. Litterst, R. Feyerherm, H.-H. Klauss, J. Magn. Magn. Mater. **290**, 302 (2005)
22. S. Sachdev, Phys. Rev. B **50**, 13006 (1994)
23. A.W. Sandvik, Phys. Rev. B **52**, R9831 (1995)
24. A.A. Belik, M. Azuma, M. Takano, Inorg. Chem. **44**, 7523 (2005)
25. R. Blinc, Phys. Rep. **79**, 331 (1981)
26. A.A. Belik, M. Azuma, M. Takano, J. Magn. Magn. Mater. **272**, 937 (2004)
27. G. Blasse, J. Phys. Chem. Solids **27**, 612 (1965)
28. M.A. Lafontaine, M. Leblanc, G. Ferey, Acta Cryst. C **45**, 1205 (1989)
29. J.C. Bonner, M.E. Fisher, Phys. Rev. **135**, A640 (1964)
30. A.N. Vasilev, JETP Lett. **69**, 876 (1999)
31. A.N. Vasilev, L.A. Ponomarenko, H. Manaka, I. Yamada, M. Isobe, Y. Ueda, Phys. Rev. B **64**, 024419 (2001)
32. H. Völenkle, A. Wittmann, H. Nowotny, Monatsh. Chem. **98**, 1352 (1967)
33. M. Braden, G. Wilkendorf, J. Lorenzana, M. Ain, G.J. McIntyre, M. Behruzi, G. Heger, G. Dhalenne, A. Revcolevschi, Phys. Rev. B **54**, 1105 (1996)
34. K. Fabricius, A. Klümper, U. Löw, B. Büchner, T. Lorenz, G. Dhalenne, A. Revcolevschi, Phys. Rev. B **57**, 1102 (1998)
35. R.M. Eremina, M.V. Eremin, V.N. Glazkov, H.-A. Krug von Nidda, A. Loidl, Phys. Rev. B **68**, 014417 (2003)
36. A.Yu. Zavidonov, I.A. Larionov, M. Itoh, Phys. Rev. B **61**, 11625 (2000)
37. A. Carpy, J. Galy, Acta Crystallogr. Sect. B **31**, 1481 (1975)
38. H. Smolinski, C. Gros, W. Weber, U. Peuchert, G. Roth, M. Weiden, C. Geibel, Phys. Rev. Lett. **80**, 5164 (1998)
39. M. Lohmann, A. Loidl, M. Klemm, G. Obermeier, S. Horn, Solid State Commun. **104**, 649 (1997)
40. P. Thalmeier, P. Fulde, Europhys. Lett. **44**, 242 (1998)
41. K.I. Kugel, D.I. Khomskii, Sov. Phys. Usp. **25**, 231 (1982)
42. I. Yamada, H. Fujii, M. Hidaka, J. Phys.: Condens. Matter **1**, 3397 (1989)
43. I. Yamada, M. Nishi, J. Akimitsu, J. Phys.: Condens. Matter **8**, 2625 (1996)
44. I. Yamada, H. Manaka, H. Sawa, M. Nishi, M. Isobe, Y. Ueda, J. Phys. Soc. Jpn. **67**, 4269 (1998)
45. Ch. Kegler, N. Büttgen, H.-A. Krug von Nidda, A. Krimmel, L. Svistov, B.I. Kochelaev, A. Loidl, A. Prokofiev, W. Aßmus, Eur. Phys. J. B **22**, 321 (2001)
46. J. Choukroun, J.L. Richard, A. Stepanov, Phys. Rev. Lett. **87**, 127207 (2001)
47. M. Oshikawa, I. Affleck, Phys. Rev. B **65**, 134410 (2002)
48. S. Tornow, O. Entin-Wohlman, A. Aharony, Phys. Rev. B **60**, 10206 (1999)
49. V. Kataev, K.-Y. Choi, M. Grüninger, U. Ammerahl, B. Büchner, A. Freimuth, A. Revcolevschi, Phys. Rev. Lett. **86**, 2882 (2001)
50. H.-A. Krug von Nidda, L.E. Svistov, M.V. Eremin, R.M. Eremina, A. Loidl, V. Kataev, A. Validov, A. Prokofiev, W. Aßmus, Phys. Rev. B **65**, 134445 (2002)
51. D. Zakharov, H.-A. Krug von Nidda, M. Eremin, J. Deisenhofer, R. Eremina, A. Loidl, in *Book Series: NATO Science for Peace and Security Series B - Physics and Biophysics: Quantum Magnetism* (Springer, Dordrecht, 2008), p. 193
52. P.W. Anderson, P.R. Weiss, Rev. Mod. Phys. **25**, 269 (1953)
53. R. Kubo, K. Tomita, J. Phys. Soc. Jpn. **9**, 888 (1954)
54. Z.G. Soos, K.T. McGregor, T.T.P. Cheung, A.J. Silverstein, Phys. Rev. B **16**, 3036 (1977)
55. B. Pilawa, J. Phys.: Condens. Matter **9**, 3779 (1997)
56. M.V. Eremin, D.V. Zakharov, R.M. Eremina, J. Deisenhofer, H.-A. Krug von Nidda, G. Obermeier, S. Horn, A. Loidl, Phys. Rev. Lett. **96**, 027209 (2006)

57. M.V. Eremin, D.V. Zakharov, H.-A. Krug von Nidda, R.M. Eremina, A. Shuvaev, A. Pimenov, P. Ghigna, J. Deisenhofer, A. Loidl, Phys. Rev. Lett. **101**, 147601 (2008)
58. C. Kegler, N. Büttgen, H.-A. Krug von Nidda, A. Loidl, R. Nath, A.V. Mahajan, A.V. Prokofiev, W. Assmus, Phys. Rev. B **73**, 104418 (2006)
59. A.D. Wadsley, Acta Crystallogr. **8**, 695 (1955)
60. H. Kobayashi, Bull. Chem. Soc. Jpn. **52**, 1315 (1979)
61. H. Yamada, Y. Ueda, J. Phys. Soc. Jpn. **68**, 2735 (1999)
62. T. Yamauchi, Y. Ueda, N. Mori, Phys. Rev. Lett. **89**, 057002 (2002)
63. G. Obermeier, D. Ciesla, S. Klimm, S. Horn, Phys. Rev. B **66**, 085117 (2002)
64. M. Itoh, N. Akimoto, H. Yamada, M. Isobe, Y. Ueda, J. Phys. Chem. Solids **62**, 351 (2001)
65. Y. Ueda, H. Yamada, M. Isobe, T. Yamauchi, J. Alloys Compd. **317-318**, 109 (2001)
66. K. Okazaki, A. Fujimori, T. Yamauchi, Y. Ueda, Phys. Rev. B **69**, 140506 (2004)
67. S. Nishimoto, Y. Ohta, J. Phys. Soc. Jpn. **70**, 309 (2001)
68. J.-I. Yamaura, M. Isobe, H. Yamada, T. Yamauchi, Y. Ueda, J. Phys. Chem. Solids **63**, 957 (2002)
69. A. Friedrich, D. Kaplan, N. Sol, R.H. Wallis, J. Phys. Lett. (France) **390**, L343 (1978)
70. T. Takahashi, H. Nagasawa, Solid State Commun. **39**, 1125 (1981)
71. H. Nagasawa, T. Takahashi, T. Erata, M. Onoda, Y. Kanai, S. Kagoshima, Mol. Cryst. Liq. Cryst. **86**, 195 (1982)
72. M. Onoda, T. Takahashi, H. Nagasawa, J. Phys. Soc. Jpn. **51**, 3868 (1982)
73. M. Onoda, H. Nagasawa, J. Phys. Soc. Jpn. **52**, 2231 (1983)
74. A.N. Vasilev, V.I. Marchenko, A.I. Smirnov, S.S. Sosin, H. Yamada, Y. Ueda, Phys. Rev. B **64**, 174403 (2001)
75. M. Heinrich, H.-A. Krug von Nidda, A. Krimmel, A. Loidl, R.M. Eremina, A. Ineev, B.I. Kochelaev, A. Prokofiev, W. Assmus, Phys. Rev. B **67**, 224418 (2003)
76. D.V. Zakharov, J. Deisenhofer, H.-A. Krug von Nidda, P. Lunkenheimer, J. Hemberger, M. Hoinkis, M. Klemm, M. Sing, R. Claessen, M.V. Eremin, S. Horn, A. Loidl, Phys. Rev. B **73**, 094452 (2006)
77. J. Deisenhofer, R.M. Eremina, A. Pimenov, T. Gavrilova, H. Berger, M. Johnsson, P. Lemmens, H.-A. Krug von Nidda, A. Loidl, K.S. Lee, M.H. Whangbo, Phys. Rev. B **74**, 174421 (2006)
78. N.D. Mermin, H. Wagner, Phys. Rev. Lett. **17**, 1133 (1966)
79. R. Bursill, G.A. Gehring, D.J.J. Farnell, J.B. Parkinson, T. Xiang, Chen Zeng, J. Phys.: Condens. Matter **7**, 8605 (1995)
80. B.J. Gibson, R.K. Kremer, A.V. Prokofiev, W. Aßmus, G.J. McIntyre, Physica B **350**, 253 (2004)
81. M. Enderle, C. Mukherjee, B. Fåk, R.K. Kremer, J.-M. Broto, H. Rosner, S.-L. Drechsler, J. Richter, J. Malek, A. Prokofiev, W. Aßmus, S. Pujol, J.-L. Raggazzoni, H. Rakoto, M. Rheinstädter, H.M. Rønnow, Europhys. Lett. **70**, 237 (2005)
82. N. Büttgen, W. Kraetschmer, L.E. Svistov, L.A. Prozorova, A. Prokofiev, Phys. Rev. B **81**, 052403 (2010)
83. N. Büttgen, H.-A. Krug von Nidda, L.E. Svistov, L.A. Prozorova, A. Prokofiev, W. Aßmus, Phys. Rev. B **76**, 014440 (2007)
84. F. Schrettle, S. Krohns, P. Lunkenheimer, J. Hemberger, N. Büttgen, H.-A. Krug von Nidda, A.V. Prokofiev, A. Loidl, Phys. Rev. B **77**, 144101 (2008)
85. M.G. Banks, F. Heidrich-Meisner, A. Honecker, H. Rakoto, J.-M. Broto, R.K. Kremer, J. Phys.: Condens. Matter **19**, 145227 (2007)
86. T. Hikihara, L. Kecke, T. Momoi, A. Furusaki, Phys. Rev. B **78**, 144404 (2008)
87. M. Mostovoy, Phys. Rev. Lett. **96**, 067601 (2006)
88. H.J. Xiang, M.-H. Whangbo, Phys. Rev. Lett. **99**, 257203 (2007)
89. H. Katsura, N. Nagaosa, A.V. Balatsky, Phys. Rev. Lett. **95**, 057205 (2005)
90. W.B. Mims, Phys. Rev. B **5**, 2409 (1972)
91. E.L. Hahn, D.E. Maxwell, Phys. Rev. **88**, 1070 (1952)
92. C. Froideveaux, M. Weger, Phys. Rev. Letters **12**, 123 (1964)
93. M. Bloom, E.L. Hahn, B. Herzog, Phys. Rev. **97**, 1699 (1955)
94. H. Abe, H. Yasuoka, A. Hirai, J. Phys. Soc. Jpn. **21**, 77 (1966)
95. A. Lombardi, M. Mali, J. Roos, D. Brinkmann, Phys. Rev. B **53**, 14268 (1996)
96. J. Degani, N. Kaplan, Phys. Rev. B **7**, 2132 (1973)
97. R. Brener, E. Ehrenfreund, J. Magn. Res. **26**, 539 (1977)
98. C.H. Pennington, D.J. Durand, C.P. Slichter, J.P. Rice, E.D. Bukowski, D.M. Ginsberg, Phys. Rev. B **39**, 274 (1989)

99. M. Lohmann, H.-A. Krug von Nidda, A. Loidl, E. Morré, M. Dischner, C. Geibel, Phys. Rev. B **61**, 9523 (2000)
100. G.S. Uhrig, Phys. Rev. B **57**, R14004 (1998)
101. A.N. Vasilev, A.I. Smirnov, M. Isobe, Y. Ueda, Phys. Rev. B **56**, 5065 (1997)
102. G. Sperlich, W.D. Lazé, Phys. Stat. Sol. B **65**, 625 (1974)
103. S.A. Altschuler, B.M. Kosyrew, *Paramagnetische Elektronenresonanz* (Teubner, Leipzig, 1963)
104. A.I. Smirnov, S.S. Sosin, V. Villar, C. Paulsen, M. Isobe, Y. Ueda, Phys. Rev. B **63**, 014412 (2000)
105. J. Das, A.V. Mahajan, J. Bobroff, H. Alloul, F. Alet, E.S. Soerensen, Phys. Rev. B **69**, 144404 (2004)
106. A. Zheludev, T. Masuda, I. Tsukada, Y. Uchiyama, K. Uchinukura, P. Böni, S.H. Lee, Phys. Rev. B **62**, 8921 (2000)
107. S.V. Demishev, Y. Inagaki, M.M. Markina, H. Ohta, S. Okubo, Y. Oshima, A.A. Pronin, N.E. Sluchanko, N.A. Samarin, V.V. Glushkov, Physica B **329-333**, 715 (2003)
108. B. Grenier, J.P. Renard, P. Veillet, L.P. Regnault, J.E. Lorenzo, C. Paulsen, G. Dhalenne, A. Revcolevschi, Physica B **259-261**, 954 (1999)
109. M. Fabrizio, R. Melin, J. Souletie, Eur. Phys. J. B **10**, 607 (1999)
110. H. Fukuyama, T. Tanimoto, M. Saito, J. Phys. Soc. Jpn. **65**, 1182 (1996)
111. D. Khomskii, W. Geertsma, M. Mostovoy, Czech. J. Phys. **46 S6**, 3239 (1996)
112. S. Miyashita, S. Yamamoto, Phys. Rev. B **48**, 913 (1993)
113. M. Hagiwara, K. Katsumata, I. Affleck, B.I. Halperin, J.P. Renard, Phys. Rev. Lett. **65**, 3181 (1990)
114. V.N. Glazkov, A.I. Smirnov, O.A. Petrenko, D. McK. Paul, A.G. Vetkin, R.M. Eremina, J. Phys.: Condens. Matter **10**, 7879 (1998)
115. V.N. Glazkov, A.I. Smirnov, G. Dhalenne, A. Revcolevschi, JETP **93**, 143 (2001)
116. S.H. Glarum, S. Geschwind, K.M. Lee, M.L. Kaplan, J. Michel, Phys. Rev. Lett. **67**, 1614 (1991)
117. S. Kimura, H. Ohta, M. Motokawa, T. Yokoo, J. Akimitsu, J. Phys. Soc. Jpn. **67**, 2514 (1998)
118. A.P. Ramirez, S.-W. Cheong, M.L. Kaplan, Phys. Rev. Lett. **72**, 3108 (1994)
119. Y. Uchiyama, Y. Sasago, I. Tsukada, K. Uchinokura, A. Zheludev, T. Hayashi, N. Miura, P. Böni, Phys. Rev. Lett. **83**, 632 (1999)
120. A.I. Smirnov, H.-A. Krug von Nidda, A. Loidl, L.N. Demianets, A. Ya. Shapiro, J. Magn. Magn. Mater. **272-276**, 880 (2004)
121. C.D. Batista, K. Hallberg, A.A. Aligia, Phys. Rev. B **60**, R12553 (1999)
122. T. Masuda, A. Fujioka, Y. Uchiyama, I. Tsukada, K. Uchinokura, Phys. Rev. Lett. **80**, 4566 (1998)
123. A.I. Smirnov, V.N. Glazkov, H.-A. Krug von Nidda, A. Loidl, L.N. Demianets, A.Ya. Shapiro, Phys. Rev. B **65**, 174422 (2002)
124. V.N. Glazkov, A.I. Smirnov, K. Uchinokura, T. Masuda, Phys. Rev. B **65**, 144427 (2002)
125. C. Yasuda, S. Todo, M. Matsumoto, H. Takayama, Phys. Rev. B **64**, 092405 (2001)
126. E. Dagotto, T. Hotta, A. Moreo, Phys. Rep. **344**, 1 (2001)
127. J.M. Tranquada, J.D. Axe, N. Ichikawa, A.R. Moodenbaugh, Y. Nakamura, S. Uchida, Phys. Rev. Lett. **78**, 338 (1997)